

1 Hotspot *ESR1* mutations are multimodal and contextual drivers of
2 breast cancer metastasis

3 Zheqi Li (1, 2), Yang Wu (2, 3), Megan E. Yates (2, 4, 5), Nilgun Tasdemir (1, 2), Amir
4 Bahreini (2, 6), Jian Chen (2), Kevin M. Levine (2, 7), Nolan M. Priedigkeit (1, 2), Simak
5 Ali (8), Laki Buluwela (8), Spencer Arnesen (9, 10), Jason Gertz (9, 10), Jennifer K.
6 Richer (11), Benjamin Troness (12), Dorraya El-Ashry (12), Qiang Zhang (13), Lorenzo
7 Gerratana (13, 14), Youbin Zhang (13), Massimo Cristofanilli (13), Maritza A. Montanez
8 (15), Prithu Sundd (15), Callen T. Wallace (16), Simon C. Watkins (16), Li Zhu (17),
9 George C. Tseng (17), Nikhil Wagle (18), Jason S. Carroll (19), Paul Jank (20), Carsten
10 Denkert (20), Maria M Karsten (21) , Jens-Uwe Blohmer (21), Ben H. Park (22), Peter C.
11 Lucas (7), Jennifer M. Atkinson (1,2), Adrian V. Lee (1, 2, 4, 6), Steffi Oesterreich (1, 2,
12 4, 6, 7)

13

14 1. Department of Pharmacology and Chemical Biology, University of Pittsburgh,
15 Pittsburgh PA, USA
16 2. Women's Cancer Research Center, Magee Women's Research Institute, UPMC
17 Hillman Cancer Center, Pittsburgh PA, USA
18 3. School of Medicine, Tsinghua University, Beijing, China
19 4. Integrative Systems Biology Program, University of Pittsburgh, Pittsburgh, PA,
20 USA.
21 5. Medical Scientist Training Program, University of Pittsburgh School of Medicine,
22 Pittsburgh, PA, USA.
23 6. Department of Human Genetics, University of Pittsburgh, Pittsburgh PA, USA
24 7. Department of Pathology, University of Pittsburgh, Pittsburgh PA, USA
25 8. Department of Surgery and Cancer, Imperial College London, London, UK
26 9. Department of Oncological Sciences, University of Utah, Salt Lake City, UT, USA

27 10. Huntsman Cancer Institute, University of Utah, Salt Lake City, UT, USA
28 11. Department of Pathology, University of Colorado Anschutz Medical Campus,
29 Aurora, CO, USA
30 12. University of Minnesota Masonic Cancer Center, Minneapolis, MN, USA
31 13. Robert H. Lurie Cancer Center of Northwestern University, Feinberg School of
32 Medicine, Chicago, IL, US
33 14. Department of Medicine (DAME) University of Udine, Udine, Italy
34 15. Pittsburgh Heart, Lung and Blood Vascular Medicine Institute, University of
35 Pittsburgh School of Medicine, Pittsburgh PA, USA
36 16. Center for Biological Imaging, University of Pittsburgh, Pittsburgh PA, USA
37 17. Department of Biostatistics, University of Pittsburgh, Pittsburgh PA, USA
38 18. Department of Medical Oncology and Center for Cancer Precision Medicine,
39 Dana-Farber Cancer Institute, Harvard Medical School, Brigham and Women's
40 Hospital, Boston, MA, USA
41 19. Cancer Research UK, Cambridge Institute, University of Cambridge, Cambridge,
42 UK
43 20. Institut of Pathology, Philipps-University Marburg, UKGM - Universitätsklinikum
44 Marburg, Marburg, Germany
45 21. Department of Gynecology with Breast Center, Charité – Universitätsmedizin
46 Berlin, Corporate member of Freie Universität Berlin, Humboldt-Universität zu
47 Berlin and Berlin Institute of Health, Berlin, Germany
48 22. Vanderbilt University Ingraham Cancer Center, Nashville, TN, USA
49

50 **Abstract (150 words)**

51 Constitutively active estrogen receptor- α (ER/ESR1) mutations have been identified in
52 approximately one third of ER+ metastatic breast cancer. Although these mutations are
53 known mediators of endocrine resistance, their potential role in promoting metastatic
54 disease has not yet been mechanistically addressed. In this study, we show the
55 presence of *ESR1* mutations exclusively in distant, but not local recurrences. In
56 concordance with transcriptomic profiling of *ESR1* mutant tumors, genome-edited
57 Y537S and D538G cell models have a reprogrammed cell adhesive gene network via
58 alterations in desmosome/gap junction genes and the *TIMP3/MMP* axis, which
59 functionally confers enhanced cell-cell contacts while decreased cell-ECM adhesion.
60 Context-dependent migratory phenotypes revealed co-targeting of Wnt and ER as
61 vulnerability. Mutant ESR1 exhibits non-canonical regulation of several metastatic
62 pathways including secondary transactivation and *de novo* FOXA1-driven chromatin
63 remodeling. Collectively, our data supports evidence for *ESR1* mutation-driven
64 metastases and provides insight for future preclinical therapeutic strategies.

65

66 **Significance (50 words)**

67 Context and allele-dependent transcriptome and cistrome reprogramming in genome-
68 edited *ESR1* mutation cell models elicit diverse metastatic phenotypes, including but not
69 limited to alterations in cell adhesion and migration. The gain-of-function mutations can
70 be pharmacologically targeted, and thus may be key components of novel therapeutic
71 treatment strategies for ER-mutant metastatic breast cancer.

72

73 **Running Title**

74 *ESR1* mutations drive breast cancer metastasis

75

76 **Key Words**

77 *ESR1* mutations, Metastasis, Cell Adhesion, Migration, Breast cancer

78

79 **Introduction**

80 More than 70% of breast cancers express estrogen receptor- α (ER/ESR1). Antiestrogen
81 therapies, including depletion of estradiol (E2) by aromatase inhibitors (AIs) or
82 antagonizing ER activity by Selective Estrogen Receptor Modulators/Degraders
83 (SERMs/SERDs), are conventional treatments for ER+ breast cancer. Development of
84 resistance to these endocrine therapies, however, remains a clinical and socioeconomic
85 challenge (1,2).

86 30-40% of endocrine-resistant metastatic breast cancer (MBC) is enriched in *ESR1*
87 somatic base pair missense mutations (3-5), that can be detected in the blood of
88 patients with advanced disease (6,7). Clinically, ligand binding domain (LBD) *ESR1*
89 mutations correlate with poor outcomes in patients with advanced disease (6,8,9).
90 Recent work from our group and others has uncovered a crucial role for these *ESR1*
91 hotspot mutations in driving constitutive ER activity and decreased sensitivity towards
92 ER antagonists (10-12). Moreover, structural investigation of the two most frequent
93 mutations, variants Y537S and D538G, has demonstrated that *ESR1* mutations stabilize
94 helix 12 (H12) in an agonist conformation, thereby providing a mechanistic explanation
95 for constitutive ER activity (13).

96 The identification of *ESR1* mutations in endocrine resistant MBC suggests that mutant
97 ER may not only mediate endocrine resistance but also have an unappreciated role in
98 enabling metastasis. Indeed, recent *in vivo* studies showed that mutant ER can promote
99 metastasis (14,15), and *in vitro* studies showed a gain of cell motility (15,16) and growth
100 in 3D culture (17). Although epithelial-mesenchymal transition (EMT) has been
101 described as one potential explanation for the Y537S mutant (18), overall mechanisms
102 remain largely unclear. In order to identify personalized therapeutic vulnerabilities in
103 patients harboring *ESR1* hotspot mutations, there is an urgent need to decipher the
104 mechanistic underpinnings and precise roles of mutant ER in the metastatic progression
105 using comprehensive approaches and model systems.

106 Previous transcriptomic profiling performed by us and others has revealed a context-
107 dependence of *ESR1* mutation effects, as well as significant differences between the
108 two most frequent hotspot mutations, Y537S and D538G (11,12,14,15,19). Differentially

109 expressed genes vary widely following expression of the mutations in their respective
110 cell line model, however, both Y537S and D538G maintain distinction from the E2-
111 dependent wild-type (WT) ER transcriptome. Similarly, comparison of the WT and
112 mutant ER cistromes has also revealed context-dependent and allele-specific effects on
113 ER recruitment (11,14). Furthermore, we recently showed that *ESR1*-mutant
114 transcriptomic reprogramming is associated with epigenetic remodeling (19). While
115 these findings imply that in the setting of high molecular diversity in tumors and patients,
116 somatic *ESR1* mutations have the potential to trigger different metastatic phenotypes,
117 this phenomenon has yet to be investigated.

118 In this study, we explore metastatic gain-of-function phenotypes in genome-edited
119 *ESR1* mutant models under the guidance of transcriptomic changes detected in clinical
120 samples. We identify mechanisms underlying context and allele-specific metastatic
121 phenotypes, and subsequently confirm alterations in a number of potential therapeutic
122 targets in metastatic tumors. We believe that our systematic bedside-to-bench approach
123 will ultimately lead to improved metastasis-free outcomes and prognosis for patients
124 with ER+ tumors.

125 **Results**

126 **Significant enrichment of *ESR1* mutations in distant metastases compared to**
127 **local recurrences**

128 To establish clinical evidence for potential metastasis-conferring roles of *ESR1* LBD
129 mutations, we compared the *ESR1* mutation frequencies between distant metastatic
130 and locally recurrent tumors. A combination of four publicly available clinical cohorts
131 (MSKCC, METAMORPH, POG570 and IEO) showed that while 156/867 distant
132 metastases (18%) harbored *ESR1* mutations, none were found in the 38 local
133 recurrence samples (Table 1 and Supplementary Table S1) (20-23). To expand upon
134 this observation, we additionally screened 75 ER+ recurrent tumors from the Women's
135 Cancer Research Center (WCRC) and Charite Hospital for *ESR1* hotspot (Y537S/C/N
136 and D538G) mutations using highly sensitive droplet digital PCR (ddPCR). We identified
137 12 *ESR1* mutation-positive cases among the distant metastases (25%), whereas none
138 of the local recurrences were *ESR1* mutation-positive (Table 1 and Supplementary
139 Table S2). Notably, there was no significant difference in time to recurrence for patients
140 with distant vs local recurrences in four of the cohorts (Supplementary Fig. S1 & Table
141 S3, data is not available for IEO cohort), excluding the possibility that the observed
142 differences could simply be due to duration of time to recurrence, as was previously
143 suggested (6).

144 ***ESR1* mutant tumors show a unique transcriptome associated with multiple**
145 **metastatic pathways**

146 To identify candidate functional pathways mediating the metastatic properties of *ESR1*
147 mutant cells, we compared WT and *ESR1* mutant tumor transcriptomes from four
148 cohorts of ER+ metastatic tumors: our local WCRC cohort (46 *ESR1* WT and 8 mutant
149 tumors) (24-26) and three previously reported cohorts - MET500 (34 *ESR1* WT and 12
150 mutants tumors), POG570 (68 *ESR1* WT and 18 mutants tumors) and DFCI (98 *ESR1*
151 WT and 32 mutants tumors) (14,22,27) (Fig. 1A & Supplementary Table S4).

152 Although principal component analyses on global transcriptomes did not segregate
153 *ESR1* WT and mutant tumors (Supplementary Fig. S2A), both "Estrogen Response

154 “Early” and “Estrogen Response Late” signatures were significantly enriched in *ESR1*
155 mutant tumors in 3 out of 4 cohorts, with a trend towards enrichment in the fourth cohort
156 (Fig. 1B). These results recapitulate the observation of ER hyperactivation as a result of
157 hotspot mutations, previously described in other preclinical studies (12,14,28).
158 Differential gene expression analysis identified a considerable number of altered genes
159 that were associated with *ESR1* mutations (Fig. 1C & Supplementary Table S5), which
160 further inferred functional alterations in various metastasis-related pathways.
161 Remarkably, “Cell-To-Cell Signaling & Interaction” and “Cell Movement” were featured
162 among the top five altered pathways for *ESR1* mutant tumors in all four cohorts (Fig.
163 1D).

164 In addition to the broad effects associated with *ESR1* mutations, we next questioned
165 whether different *ESR1* mutant variants could display divergent functions. A meta-
166 analysis of the five above-mentioned ER+ MBC cohorts examining *ESR1* mutations
167 underscored D538G (37%) and Y537S (24%) as the predominant variants (Fig. 1E).
168 Given the challenge of merging RNA-seq data sets from multiple cohorts due to
169 immense technical variations, we selectively compared mutation variant specific
170 transcriptomes of ten Y537S- or eight D538G-harboring tumors to the WT counterpart
171 (n=32) respectively from the DFCI cohort, which provided the largest numbers and thus
172 maximized statistical power. Aligning enrichment levels of 50 hallmark gene sets for the
173 two mutant variants again confirmed “Estrogen Response Early” and “Estrogen
174 Response Late” as the top co-upregulated pathways (Fig. 1F), with Y537S tumors
175 displaying higher ER activation (Supplementary Fig. S2B), consistent with cell line
176 studies (12,29). We also identified enriched cell cycle related pathways (E2F targets,
177 G2M checkpoint and mitotic spindle) and metabolic related pathways (fatty acid, bile
178 acid and xenobiotic metabolisms) in Y537S and D538G tumors, respectively, implying
179 that different *ESR1* mutant variants might hijack distinct cellular functions to promote
180 malignancy. Taken together, these results provide support that despite mutant variant-
181 specific alterations, *ESR1* mutations might broadly mediate metastatic phenotypes
182 through effects on cell-to-cell interactions and cell movement. We next validated the *in*
183 *silico* results using previously established genome-edited MCF7 and T47D cell line
184 models (12).

185 **ESR1 mutant-cells exhibit stronger cell-cell adhesion**

186 We first addressed the enrichment of cell-cell interaction signaling in the mutant tumors
187 through morphological inspection of cell cluster formation in suspension culture (Fig.
188 2A). We observed more compact cell clusters in MCF7 and T47D mutant cell lines
189 compared to their WT counterparts after six days of suspension culture. A time course
190 study confirmed enhanced cluster formation 24-48hrs past cell seeding (Supplementary
191 Fig. S3A). Similar observations were made in individual clones, eliminating the
192 possibility for clonal effects (Supplementary Fig. S3B).

193 Since *ESR1* mutant cells displayed significantly increased ligand-independent growth in
194 suspension (Fig. 2B), we sought to rule out the possibility that increased cluster
195 formation was simply a result of increased cell number by assessing cell-cell adhesive
196 capacity using multiple approaches in short term culture (within 1 day). We therefore
197 directly quantified homotypic cell-cell interactions by measuring the adhesion of calcein-
198 labelled *ESR1* WT or mutant cells. This assay showed that both MCF7 mutant cells
199 exhibited significantly stronger cell-cell adhesion compared to the WT cells (Fig. 2C). In
200 T47D cells, a similar effect was observed, but was limited to the T47D-Y537S mutant
201 cells (Supplementary Fig. S4A). These assays were complemented by quantification of
202 cell aggregation rates as a direct reflection of cell-cell adhesion, which confirmed faster
203 aggregation in MCF7-Y537S/D538G and T47D-Y537S cells (Fig. 2D & Supplementary
204 Fig. S4B-S4D). In addition, these stronger cell-cell adhesive properties were also
205 reproduced in additional *ESR1* mutant cell models from other laboratories (19,28)
206 (Supplementary Fig. S4E and S4F).

207 Cell-cell interaction has been reported to affect several stages of metastasis, including
208 collective invasion, intravasation, dissemination and circulation (30-32). To test whether
209 ER mutations may affect tumor cell-cell adhesion in circulation, we utilized a microfluidic
210 pump system to mimic arterial shear stress. Comparing representative images before
211 and after 2 hours of microfluidic flow, we found MCF7 *ESR1* mutant cells had a greater
212 tendency to aggregate together (Fig. 2E and 2F). Larger clusters comprised of five or
213 greater cells were more prevalent in the *ESR1* mutant cell lines, whereas smaller two-

214 cell clusters were diminished (Fig. 2G). A similar phenotype was also identified in
215 additional MCF7 *ESR1* mutant cells and in our T47D-Y537S cell line (Supplementary
216 Fig. S5A-S5I), consistent with our observations in static conditions. In an additional
217 orthogonal approach, we utilized a quantitative microfluidic fluorescence microscope
218 system simulating blood flow (33). Quantification of dynamic adhesion events
219 normalized to adhesion surfaces revealed a consistent enhanced cell-cell adhesion
220 capacity of *ESR1* mutant MCF7 cells (Supplementary Fig. S5J-S5K, Supplementary
221 videos 1-3). Together, these results show that hotspot *ESR1* mutations confer
222 increased cell-cell attachment under static and fluidic conditions, and that the effect size
223 is dependent upon mutation type and genetic backgrounds. These findings are at odds
224 with increased EMT features (18), and indeed the majority of *ESR1* mutant models and
225 tumors did not show increased EMT signature or increased expression of EMT marker
226 genes (Supplementary Fig. S6).

227 We next sought to assess whether this unexpected phenotype translated into numbers
228 of CTC clusters and subsequent metastasis *in vivo*. One hour post intracardiac injection
229 into athymic mice, circulating MCF7 WT and mutant cells were enriched from blood
230 using a previously described electrical CTC filtering method (34) (Fig. 2H). 41%-81% of
231 CTC clusters were composed of both cancer and non-cancer cells (Supplementary Fig.
232 S7A). Despite no difference in the average amount of single CTCs and CTC clusters
233 per mouse between the WT and mutant *ESR1* (Supplementary Fig. S7B & S7C), we
234 found that overall MCF7-Y537S mutant cells were significantly enriched in clusters with
235 greater than 2 cells (Fig. 2I). Furthermore, quantification of inter-nuclei distances
236 between two-cell clusters revealed denser MCF7-Y537S clusters (Fig. 2J), supporting
237 stronger MCF7-Y537S cell-cell interactions in an *in vivo* blood circulation environment.
238 The data from the MCF7-D538G mutant cells did not recapitulate the adhesive
239 phenotype we discerned *in vitro*, suggesting mutation site-specific interactions with the
240 *in vivo* microenvironment potentially affect cluster formation.

241 We next performed tail vein injection and monitored bloodborne metastatic development
242 in longer-term *in vivo* experiments without estradiol supplement (Fig. 2K). We observed
243 multiple distant macro-metastatic tumors in 4/6 (67%) MCF7-Y537S mutant cell-injected

244 mice (Fig. 2L). In contrast, distant macro-metastatic tumor was observed in only one
245 mouse of MCF7-D538G group (1/7) and none in MCF7-WT group (0/7) (Fig. 2M, left
246 panel). We detected no difference in lung micro-metastatic foci areas between WT and
247 mutant cell-injected mice, potentially due to a high baseline of MCF7 lung colonization
248 capacity (Fig. 2M, right panel). In contrast to our MCF7 results, we only discerned
249 macro-metastatic tumors from each T47D mutant group (Y537S: 1/6; D538G: 1/7) and
250 none in T47D-WT group (0/7) after 23 weeks of injection (Fig. 2O, left panel),
251 underpinning its less aggressive behavior as compared to MCF7 cells (35,36). However,
252 both T47D-Y537S and T47D-D538G mutant cells resulted in enlarged lung micro-
253 metastases, with a more pronounced effect in the T47D-D538G cells (Fig. 2N and 2O,
254 right panel). Interestingly, our *in vitro* assays did not suggest altered cell-cell adhesion in
255 the T47D-D538G model, suggesting the potential use of alternative mechanisms to
256 strengthen its metastatic properties *in vivo*.

257 Encouraged by our *in vitro* and *in vivo* findings, we next examined CTC clusters in
258 patients with *ESR1* mutant tumors. Taking advantage of a recent CTC sequencing
259 study (37), we sought to generate CTC cluster gene signatures. Differential gene
260 expression analysis in two patients with ER+ disease who had at least two CTC clusters
261 and single CTCs sequenced identified CTC cluster enriched genes (Supplementary Fig.
262 S8A and Table S6), which we subsequently applied to our RNA-seq dataset with 51
263 pairs of ER+ primary-matched metastatic tumors (44 *ESR1* WT and 7 mutant) merged
264 from the WCRC and DFCI cohorts. *ESR1* mutant metastatic tumors exhibited
265 significantly higher enrichment of CTC cluster-derived gene signatures (Supplementary
266 Fig. S8B).

267 To examine the interplay between *ESR1* mutations status, numbers of CTCs, and
268 clinical outcome, we analyzed a cohort of 151 patients with MBC. Median age at the first
269 blood draw for CTCs enumeration was 55 years (IQR: 44 - 63 years), 63 patients
270 (45.7%) were diagnosed with ER+ MBC, 37 (26.8%) with HER2-positive MBC and 38
271 (27.5%) with TNBC. Bone (49.7%), lymph nodes (41.1%), lung (34.4%) and liver (34%)
272 were the most common sites of metastasis (Supplementary Table S7). Median number
273 of CTCs was 1 (IQR: 0-10), clusters were detectable in 14 patients (9.3%) (Fig. 2P) and

274 in this subgroup the median number of clustered CTCs was 15.5 (IQR: 4 - 20).
275 Classifying the MBC by CTC numbers, with CTC \geq 5/7.5ml blood being more
276 aggressive, and CTC<5/7.5 ml blood more indolent, there were 101 Stage IV indolent
277 (69.9%) and 50 Stage IV aggressive cases (33.1%) in the study. If cases were classified
278 by presence of CTC clusters in blood, there were 10 (6.6%) and 141 (93.4%) cases
279 with >4 CTC clusters and ≤ 4 clusters, respectively. (Supplementary Table S7).
280 Mutations in hotspots D538 and Y537 of *ESR1* were detected in 30 patients (19.9%),
281 while mutations in hotspots E453 and H1047 of *PIK3CA* were detected in 40 patients
282 (26.5%) (Supplementary Table S7). A significant association was observed between
283 *ESR1* genotype status and clustered CTCs > 4 ($P = 0.027$) (Fig. 2Q), while no
284 association was observed with respect to *PIK3CA* ($P=0.725$). Notably, patients with > 4
285 CTCs clusters experienced the worse prognosis in terms of OS (6 months OS: 12.7%)
286 both with respect to those without clusters (6 months OS: 88.5%) and those with
287 clusters but with ≤ 4 clustered CTCs (6 months OS: 100%) ($P < 0.0001$) (Fig. 2R).

288 **Mutant *ESR1* cells show increased desmosome gene and gap junction gene
289 families**

290 To elucidate the mechanism of enhanced cell-cell adhesion, we investigated the
291 enrichment of four major cell-cell junction subtypes – desmosomes, gap junctions
292 (connexons), tight junctions and adherens junctions within the cell model RNA-seq data
293 (12) (Supplementary Table S6). Enrichment of the desmosome gene and gap junction
294 gene families was observed in both MCF7-Y537S/D538G and T47D-Y537S cells (Fig.
295 3A). Tight junctions were enriched in WT cells, and there were no differences in the
296 adherens junction gene family expression (Supplementary Fig. S9A). Individual gene
297 expression analysis ($FC > 1.2$, $p < 0.05$) identified 18 commonly upregulated desmosome
298 genes and 4 gap junction genes in both MCF7 *ESR1* mutant cell lines (Fig. 3B). In
299 addition to keratins, induction of classical desmosome genes *DSC1/2*, *DSG1/2* and
300 *PKP1*, and gap junction genes *GJA1*, *GJB2* and *GJB5* were observed and validated by
301 qRT-PCR in MCF7 cells (Fig. 3D). Higher protein levels were also observed for *DSC1*,
302 *DSG2*, *PKP1*, *GJA1* (Cx43), and *GJB2* (Cx26) (Fig. 3C). Immunofluorescence staining

303 revealed significantly higher *DSG2* expression in MCF7-Y537S at cell-cell contact
304 surfaces, with a trend observed in MCF7-D538G (Fig. 3E). Consistent with the weaker
305 *in vitro* cell-cell adhesion phenotypes in T47D mutant cells, we observed less
306 pronounced desmosome and gap junction gene expression changes in T47D-Y537S
307 cells (Supplementary Fig. S9B). We validated the overexpression of the key
308 desmosome and gap junction genes in RNA-seq datasets from seven additional *ESR1*
309 mutant cell models and performed further validation studies in two of them
310 (Supplementary Fig. S9C-S9E) (11,15,19). Moreover, mining RNA-seq data from
311 recently reported *ESR1* WT and mutant *ex vivo* CTC models (38), we observed
312 overexpression of three gap junction and desmosome genes in the *ESR1* mutant CTC
313 lines (Supplementary Fig. S9F). Finally, the top upregulated desmosome and gap
314 junction genes (Supplementary Table S6) were also found significantly enriched in intra-
315 patient matched primary and metastatic lesions with *ESR1* mutations (Fig. 3F).

316 We next investigated the functional roles of the reprogrammed adhesome in the *ESR1*
317 mutant MCF7 cells. Transient individual knockdown of *DSC1*, *DSC2*, *GJA1* or *GJB2* did
318 not cause significant changes in adhesion in either *ESR1* mutant line (Supplementary
319 Fig. S10A). However, we found compensatory effects observed in the desmosome and
320 gap junction knockdowns as exemplified by increased *GJA1* levels after *DSC1* or *DSC2*
321 knockdown (Supplementary Fig. S10B). The adhesive phenotype was disrupted,
322 however, with an irreversible pan-gap junction inhibitor, Carbenoxolone (CBX), or with
323 blocking peptide cocktails against desmocollin1/2 and desmoglein1/2 proteins. Both
324 treatments caused significant inhibition of cell-cell aggregation in static conditions
325 (Supplementary Fig. S10C & S10D) as well as diminished cluster propensities and size
326 in microfluidic conditions (Fig. 3G-3L), suggesting redundancy in the mutant-driven
327 reprogrammed desmosome and connexon pathways. In summary, MCF7-
328 Y537S/D538G and T47D-Y537S mutants showed increased expression of desmosome
329 and gap junction gene family components, which contributes to our observed enhanced
330 cell-cell adhesion phenotype.

331 We next investigated the mechanisms underlying the elevated desmosome and gap
332 junction components in *ESR1* mutant cells. Because hotspot *ESR1* LBD mutations are

333 well-described as conferring constitutive ER activation, we first examined if these cell-
334 cell adhesion target genes are direct outcomes of ligand-independent transcriptional
335 programming. Interrogating publicly available RNA-seq and microarray datasets of six
336 estrogen treated ER+ breast cancer cell lines (12,39-41), we found limited and
337 inconsistent E2 induction of all examined cell-cell adhesion genes when compared to
338 classical E2 downstream targets such as *GREB1* and *TFF1* (Supplementary Fig. S11A).
339 Surprisingly, mining our MCF7 *ESR1* mutant cell model ER ChIP-seq data (42) showed
340 an absence of proximate Y537S or D538G mutant ER binding sites (\pm 50kb of TSS) at
341 desmosome and connexon target gene loci. These results suggest that the
342 reprogrammed cell-cell adhesome is not a direct consequence of mutant ER genomic
343 binding.

344 We therefore hypothesized that these altered adhesion target genes might be regulated
345 via a secondary downstream effect of the hyperactive mutant ER. A seven-day siRNA
346 ER knockdown assessment identified *GJA1* as the only target gene that could be
347 blocked in mutant cells following ER depletion, whereas, strikingly, *DSC1*, *DSG1*, *GJB2*
348 and *GJB5* mRNA levels were increased in all cell lines (Fig. 3M). This was congruent
349 with *ESR1* knockdown in five additional ER+ parental cell lines, with the majority
350 exhibiting a decrease in *GJA1* expression levels (Supplementary Fig. S11B). To unravel
351 potential intermediate transcription factors (TFs) involved in the secondary regulation,
352 we examined the levels of TFs previously reported to regulate *GJA1* expression (43)
353 (Supplementary Fig. S11C). Among those, the AP1 family component *FOS* (cFos) was
354 identified as the top TF upregulated in *ESR1* mutant cells in a ligand-independent
355 manner. In addition, the AP1-associated transcriptional signature was also significantly
356 enriched in MCF7 *ESR1* mutant cells (Supplementary Fig. S11D), and hence we tested
357 if *GJA1* overexpression was dependent on the cFOS/AP1 transcriptional network.
358 Higher cFOS mRNA and protein levels in *ESR1* mutant cells were confirmed, which
359 declined along with *GJA1* levels after *ESR1* knockdown (Fig. 3N & Supplementary Fig.
360 S11E). Importantly, pharmacological inhibition of cFOS-DNA binding partially rescued
361 *GJA1* overexpression in *ESR1* mutant cells (Fig. 3O, Supplementary Fig. S11F-S11G).
362 In conclusion, our results denote *GJA1* as an indirect target of mutant ER through
363 activation of the cFOS/AP1 transcriptional axis in MCF7 cell models.

364 Since the majority of the cell-cell adhesion targets altered in the *ESR1* mutant cells
365 were not direct ER target genes (Supplementary Fig. S11A & S11B), we investigated
366 potential impacts of epigenetic remodeling on these targets. Using our recently reported
367 ATAC-seq dataset from T47D *ESR1* mutant cells (19), we observed that one of the
368 connexon targets, *GJB5*, exhibited increased chromatin accessibility at its gene locus in
369 T47D-Y537S cells (Supplementary Fig. S12A & S12B), suggesting that epigenetic
370 activation modulates gene expression in this particular context. We further evaluated
371 active histone modifications on our target gene loci in the MCF7 model. We observed
372 enhanced H3K27ac and H3K4me2 recruitment in both MCF7-Y537S and D538G cells
373 at the nearest two histone modification sites around the *DSC1* and *DSG1* loci, the two
374 most upregulated desmosome component genes in MCF7 mutant cells (Fig. 3P),
375 suggesting activation of desmosome genes via an indirect ER-mediated epigenetic
376 activation (Fig. 3Q).

377 ***ESR1* mutations promote reduced adhesive and enhanced invasive properties via
378 altered *TIMP3-MMP* axis**

379 In addition to altered cell-cell adhesion, metastasis is also mediated by coordinated
380 changes in cell-matrix interaction (44,45). Therefore, we assessed whether mutant ER
381 affects interaction with the extracellular matrix (ECM). Computational analysis showed
382 inverse correlation between ECM receptor pathway signatures and *ESR1* mutation
383 status in the DFCI cohort with the same trend appearing in 2/3 of the remaining cohorts
384 (Fig. 4A, Supplementary Fig. S13A & Table S6). Employing an adhesion array on seven
385 major ECM components, we observed that the MCF7 *ESR1* mutant cell lines
386 consistently lacked adhesive properties on almost all ECM components with the
387 exception of fibronectin, and T47D *ESR1* mutant cells displayed reduced adhesion on
388 collagen I, collagen II and fibronectin (Fig. 4B). Considering that collagen I is the most
389 abundant ECM component in ER+ breast cancer (Supplementary Fig. S13B), we
390 repeated the adhesion assay on collagen I (Fig. 4C & 4D; Supplementary Fig. S13C &
391 S13D) and similarly found reduced adhesion in both ER mutant cells. In an orthogonal
392 approach, we visualized and quantified adhesion in a co-culture assay on collagen I
393 using differentially labelled *ESR1* WT and mutant cells, which confirmed significantly

394 decreased adhesive properties in the mutant cells (Supplementary Figure S13E &
395 S13F). Of note, *ESR1* mutant adhesion deficiency on collagen I was also observed in
396 two additional *ESR1* mutant models (Supplementary Fig. S13G).

397 We sought to investigate the molecular mechanisms underlying the unique defect of
398 collagen I adhesion in *ESR1* mutant cells. There was no consistent change in
399 expression of members of the integrin gene family, encoding well-characterized direct
400 collagen I adhesion receptors, in our cell line models (Supplementary Fig. S14A and
401 Supplementary Table S6). We therefore hypothesized that another gene critical in
402 regulation of ECM genes might be altered and to test this directly, we performed gene
403 expression analysis of 84 ECM adhesion-related genes using a qRT-PCR array
404 (Supplementary Table S8). Pairwise comparisons between each mutant cell line and
405 corresponding WT cells revealed a strong context-dependent pattern of ECM network
406 reprogramming, with more pronounced effects in MCF7 cells (Fig. 4E). Intersection
407 between Y537S and D538G mutants showed 23 and 1 consistently altered genes in
408 MCF7 and T47D cells, respectively (Fig. 4F). *TIMP3*, the gene encoding tissue
409 metallopeptidase inhibitor 3, was the only shared gene between all four mutant cell
410 models (Fig. 4F), and we confirmed its decreased expression at the mRNA (Fig. 4G &
411 Supplementary Fig. S14B) and protein level (Fig. 4H), as well as in other genome-
412 edited *ESR1* mutant models (Supplementary Fig. S14C). E2 treatment represses
413 *TIMP3* expression, suggesting that it's downregulation in *ESR1* mutant cells is likely due
414 to ligand-independent repressive ER activity (Supplementary Fig. S14C).
415 Overexpression of *TIMP3* rescued the adhesion defect in *ESR1* mutant cells (Figure 4I,
416 4J & Supplementary Fig. S14D), with no impact on cell proliferation (Supplementary Fig.
417 S14E). Collectively, these data imply a selective role for *TIMP3* downregulation in
418 causing the decreased cell-matrix adhesion phenotype of the *ESR1* mutant cells,
419 consistent with a critical role for *TIMP3* in metastasis in other cancer types (46,47).

420 Given the role of *TIMP3* as an essential negative regulator of matrix metalloproteinase
421 (MMP) activity (48), we compared MMP activity between *ESR1* WT and mutant cells. A
422 pan-MMP enzymatic activity assay revealed significantly increased MMP activation in all
423 mutant cells (Fig. 4K & 4L), indicating that the *ESR1* mutant cells have increased

424 capacity for matrix digestion. This was validated in spheroid-based invasion assays in
425 which cells were embedded in collagen I (Fig. 4M) but without notable growth
426 differences (Supplementary Fig. S15A & S15B). This was additionally visualized in co-
427 culture spheroid invasion assays using differentially labelled T47D *ESR1* WT and
428 mutant cells, which showed an enrichment of *ESR1* mutant cells at the leading edge of
429 the spheroids (Supplementary Fig. S15C). Lastly, we tested if MMP blockade could
430 repress the *ESR1* mutant-driven invasiveness. Marimastat treatment substantially
431 reduced the invasive phenotype of *ESR1* mutant cells in a dose dependent manner (Fig.
432 4N-4Q). These data demonstrate that decreased TIMP3 expression, resulting in
433 increased MMP activation causes enhanced matrix digestion associated with decreased
434 adhesion to ECM, ultimately conferring invasive properties to *ESR1* mutant cells.

435 ***De novo* FOXA1-mediated Wnt pathway activation enhances of the T47D-D538G**
436 **cell migration**

437 T47D D538G cells showed increased *in vivo* tumorigenesis despite showing less
438 pronounced adhesive phenotypes compared to T47D Y537S and MCF7 Y537S/D538G
439 cells. Reasoning mutation and context-dependent metastatic activities of the mutant ER
440 protein and having identified “Cellular Movement” as another top hit in our initial
441 pathway analysis of differentially expressed genes in *ESR1* mutant tumors (Fig. 1D), we
442 assessed potential differences in cellular migration between the different models.
443 Wound scratch assays identified significantly increased cell motility in the T47D-D538G
444 model (Fig. 5A & 5B), but not in T47D-Y537S (Fig. 5B) or MCF7 mutant cells
445 (Supplementary Fig. S16A & S16B). This enhanced motility was shared between the
446 three individual T47D-D538G clones again excluding potential clonal artifacts
447 (Supplementary Fig. S16C & S16D). Furthermore, we observed a different morphology
448 of T47D-D538G cells at the migratory leading edges (Fig. 5C) further confirmed by
449 larger and stronger assembly of F-actin filaments at the edge of T47D-D538G cell
450 clusters (Supplementary Fig. S16E-S16H). To mimic collective migration from a cluster
451 of cells, we utilized a spheroid-based collective migration assay on type I collagen (Fig.
452 5D). The distance to the leading edges of T47D-D538G mutant cells was significantly
453 longer compared to WT spheroids (Fig. 5E). In orthogonal approaches, enhanced

454 migratory capacities of T47D-D538G cells were observed in co-culture assay using
455 labelled T47D-WT and D538G cells (Supplementary Fig. S16I & S16J) and in Boyden
456 chamber transwell assays (Supplementary Fig. S16K & S16L). Finally, in T47D
457 overexpression models, we also observed significantly enhanced migration in D538G
458 compared to WT overexpressing cells (Supplementary Fig. S17).

459 To understand the mechanisms underlying the migratory phenotype of T47D-D538G
460 cells we identified pathways uniquely enriched in these cells. GSEA identified endocrine
461 resistance-promoting pathways (e.g. E2F targets) in both T47D mutants, whereas Wnt-
462 β -catenin signaling was one of the uniquely enriched pathways in T47D-D538G (Fig.
463 5F). Hyperactivation of the canonical Wnt- β -catenin pathway was further confirmed by a
464 Top-Flash luciferase assay (Supplementary Fig. S18A). We also observed increased
465 phosphorylation of GSK3 β and GSK3 α as well as β -catenin (both total and nuclear)
466 protein levels in T47D-D538G cells (Fig. 5G and Supplementary Fig. S18B). To address
467 the potential clinical relevance of these findings, we utilized the porcupine inhibitor
468 LGK974, which prevents the secretion of Wnt ligands and is currently being tested in a
469 clinical trial for patients with advanced solid tumors including breast cancer
470 (NCT01351103) (49,50). Treatment with LGK974 resulted in a 20% and 40% inhibition
471 of T47D *ESR1* WT and D538G mutant cell migration respectively (Fig. 5H and
472 Supplementary Fig. S18C) yet had no effect on cell proliferation (Supplementary Fig.
473 S18D). We next studied the combination of LGK974 and the selective ER degrader
474 (SERD), Fulvestrant, in migration assays, in which we detected significant synergy (Fig.
475 5I), suggesting that combination therapy co-targeting the Wnt and ER signaling
476 pathways might reduce the metastatic phenotypes of Wnt hyperactive *ESR1* mutant
477 tumors.

478 We sought to decipher the mechanisms underlying T47D-D538G Wnt hyperactivation.
479 Comparing the fold changes of canonical Wnt signaling positive regulators between
480 T47D-Y537S and T47D-D538G mutant cells, we identified eight candidate genes
481 exhibiting pronounced enrichment in T47D-D538G cells (Fig. 5J), including ligands (e.g.
482 *WNT6A*), receptors (e.g. *LRP5*) and transcriptional factors (e.g. *TCF4*). With the
483 exception of *LRP5*, none of these candidate genes were induced by E2 stimulation in

484 T47D *ESR1* WT cells (Supplementary Fig. S19A). Lack of consistent E2 regulation was
485 confirmed in five additional ER+ breast cancer cell lines (Supplementary Fig. S19B).
486 Hence, we alternatively hypothesized that D538G ER might gain *de novo* binding sites
487 proximal to Wnt pathway genes allowing their induction. We mapped ER binding
488 globally by analyzing ER ChIP-sequencing in T47D WT and *ESR1* mutant cells.
489 Consistent with previous studies (14,28), mutant ER were recruited to binding sites
490 irrespective of hormone stimulation (Supplementary Fig. S19C & Table S9). However,
491 none of the mutant ER bound regions mapped to identified Wnt pathway genes (\pm 50kb
492 of TSS), again suggesting a lack of direct canonical ER regulation. Moreover, short-term
493 fulvestrant treatment only weakly damped T47D-D538G cell migration (Fig. 5K & 5M)
494 suggesting that ER activation may not be an essential prerequisite for enhanced cell
495 migration in D538G cells.

496 Given our recent findings of enriched FOXA1 motifs in gained open chromatin of T47D-
497 D538G cells (19), we decided to validate this pivotal *in silico* prediction, focusing on our
498 observed migratory phenotype. In contrast to the limited effects of ER depletion,
499 strikingly, FOXA1 knockdown fully rescued the enhanced migration in T47D-D538G
500 cells (Fig. 5L & 5N), indicating a more dominant role of FOXA1 in controlling T47D-
501 D538G cell migration. Ligand-independent 2D growth of T47D-D538G cells was
502 inhibited by both fulvestrant and FOXA1 knockdown (Supplementary Fig. S19D),
503 suggesting a canonical ER-FOXA1 co-regulatory mechanism in growth, distinguished
504 from the role of FOXA1 in the regulation of migration.

505 To further explore how FOXA1 contributes to the migratory phenotype, we performed
506 FOXA1 ChIP-sequencing to decipher the genomic binding profiles. We identified
507 approximately 30,000 peaks in T47D WT cells regardless of E2 stimulation and a \sim 1.6
508 fold increase in binding sites of the Y537S (61,934) and D538G (54,766) ER mutants
509 (Supplementary Fig. S20A & Supplementary Table S9). PCA distinctly segregated all
510 four groups (Fig. 5O), suggesting unique FOXA1 binding site redistribution. Comparison
511 of binding intensities revealed 14%, 28% and 21% FOXA1 binding sites were altered in
512 WT+E2, Y537S and D538G groups, respectively, with a predominant gain of binding
513 intensities in the two T47D mutants (Fig. 5P and Supplementary Fig. S20B).

514 Since FOXA1 is a well-known essential pioneer factor of ER in breast cancer, we
515 examined interplay between FOXA1 and WT and mutant ER. Interestingly, both Y537S
516 (39%) and D538G (25%) ER binding sites showed a significantly lower overlap between
517 FOXA1 compared to the WT+E2 group (56%), albeit with the increased number of
518 gained mutant FOXA1 binding sites (Supplementary Fig. S20C). This discrepancy
519 suggests that FOXA1 exhibits a diminished ER pioneering function and instead might
520 contribute to novel functions via gained *de novo* binding sites. Co-occupancy analysis
521 using isogenic ATAC-seq data (19) uncovered that the open chromatin of T47D-D538G
522 cells was more associated with FOXA1 binding sites compared to WT and T47D-Y537S
523 cells (Fig. 5Q). FOXA1 binding intensities were also stronger in D538G ATAC-sites
524 (Supplementary Fig. S20D). Collectively, these results provide evidence that FOXA1
525 likely plays a critical role in the D538G mutant cell to reshape its accessible genomic
526 landscape.

527 We further investigated the impact of the gained FOXA1-associated open chromatin on
528 transcriptomes, particularly exploring *ESR1* mutant-specific genes. Intersection of the
529 gained FOXA1- and ATAC-sites for annotated T47D-D538G genes with non-canonical
530 ligand-independence identified 25 potential targets that could be attributed to *de novo*
531 FOXA1 bound open chromatin, exemplified by *PRKG1* and *GRFA* as top targets (Fig.
532 5R & Supplementary Fig. S21A). Notably, one of our identified D538G specific Wnt
533 regulator genes, *TCF4*, was uncovered in this analysis. Higher *TCF4* expression in
534 T47D-D538G cells was validated by qRT-PCR and furthermore this increased
535 expression could be fully blocked following FOXA1 knockdown (Supplementary Fig.
536 S21B). Additionally, stronger FOXA1 recruitment at the *TCF4* gene locus was validated
537 via ChIP-qPCR (Supplementary Fig. S21C and S21D). Importantly, overexpression of
538 dominant negative *TCF4* strongly impaired cell migration in T47D-D538G, while it only
539 slightly affected WT cells (Fig. 5S). Together, these results support that FOXA1 binding
540 site redistribution leads to novel chromatin remodeling and enhanced expression of
541 genes with roles in metastases including *TCF4*, which subsequently activate Wnt-driven
542 migration in T47D-D538G cells.

543

544 **Discussion**

545 Hotspot somatic mutations clustered in the LBD of ER represent a prevalent molecular
546 mechanism that drives antiestrogen resistance in ~30% of advanced ER+ breast cancer.
547 There is an urgent need for a deeper understanding of this resistance mechanism in
548 order to develop novel and personalized therapeutics. Utilizing clinical samples, *in silico*
549 analysis of large datasets, and robust and reproducible experimentation in multiple
550 genome-edited cell line models, our study uncovers complex and context-dependent
551 mechanisms of how *ESR1* mutations confer gain-of-function metastatic properties. We
552 identified *ESR1* mutations as multimodal metastatic drivers hijacking adhesive and
553 migratory networks, and thus likely influencing metastatic pathogenesis and progression.
554 Mechanistically, we uncovered novel ER-indirect regulation of metastatic candidate
555 gene expression, distinct from previously described (11,12,51) canonical ligand-
556 independent gene induction (Fig. 6). Nonetheless, some limitations were noted in our
557 study, such as the lack of *in vivo* validation of studied therapeutic approaches. In
558 addition, our numbers for clinical samples of paired primary-metastatic tumors harboring
559 *ESR1* mutations is finite, necessitating validation in future studies with larger clinical
560 cohorts.

561 We discovered enhanced cell-cell adhesion via upregulated desmosome and gap
562 junction networks in cell lines and clinical samples with *ESR1* mutations. These
563 transcriptional alterations are associated with a specific clinical phenotype characterized
564 not only by treatment resistance, but also by high CTC count and a different metastatic
565 organotropism (52,53). We propose that this key alteration may support increased
566 metastases in ER mutant tumors through facilitating the formation of homo- or
567 heterotypic CTC clusters, providing a favorable environment for CTC dissemination, as
568 previously described (30). This idea is further supported by previous data showing
569 upregulation of the desmosome gene plakoglobin (*JUP*) and cytokeratin 14 (*KRT14*),
570 which may play a role in a CTC cluster formation signature (30,54). We observed
571 increased expression of plakophilin, desmocollin, and desmoglein in *ESR1* mutant cells,
572 suggesting the importance of the broad desmosome network reprogramming for
573 functional cell clustering activity. Moreover, enhanced gap junction genes might

574 potentiate intercellular calcium signaling, facilitating the prolonged survival of various
575 metastatic cell types tethered to *ESR1* mutant cells *en route* (55). Dissociation of CTC
576 cluster using Na⁺/K⁺ ATPase inhibitors decreased metastasis *in vivo* (37). In addition,
577 previous studies have validated the anti-tumor effects of FDA-approved gap junction
578 blockers carbenoxolone and mefloquine *in vivo* (56,57). Our results warrant additional
579 preclinical studies using drugs targeting desmosome and gap junctions, with the
580 ultimate goal of applying these treatments in a CTC-targeted clinical trial to improve
581 outcomes for patients harboring breast cancers with *ESR1* mutations.

582 Previous studies using similar *ESR1* mutant cell models described enhanced migratory
583 properties (15,16), but no mechanistic explanations were uncovered. Here we identify a
584 critical role for Wnt-β-catenin signaling and show that co-targeting of Wnt and ER
585 resulted in synergistic inhibition of cell migration. Intriguingly, the strong effect we
586 observed on migration was unique to T47D-D538G cells, a discovery that was made
587 possible through our use of multiple genome-edited mutation models. This finding might
588 help explain the higher frequency of D538G mutations in metastatic samples, despite
589 the stronger endocrine resistance phenotype of Y537S mutation (5,12,14,29,58). Of
590 note, slightly higher Wnt activity and β-catenin accumulation were also observed in
591 T47D-Y537S cells, but this failed to convert into a migratory phenotype. It is possible
592 that some genes uniquely regulated by Y537S ER in T47D cells might inhibit migratory
593 phenotypes. For instance, the gap junction component, connexin 43, which is
594 exclusively upregulated in T47D-Y537S cells, has been reported to play an inhibitory
595 role in epithelial cell migration (59). *In vivo* experiments revealed striking enhancement
596 of metastatic capacity in the MCF7-Y537S but not D538G model. This discrepancy with
597 *in vitro* data could possibly be explained by the longer distant metastatic latency
598 requirement of D538G cells *in vivo*, consistent with a recent study using overexpression
599 cell models (14). These data support strong allele and context dependent effects of the
600 *ESR1* mutation on metastatic phenotypes, in line with context dependent effects on
601 transcriptome, cistromes and accessible genome in *ESR1* mutant cells (11,12,14,19).
602 Of note, previous efforts using multiple cell line models with *ESR1* mutations elucidated
603 several congruent molecular and functional alterations associated with endocrine
604 resistance (14,15,51,58), suggesting that mechanisms underlying metastasis of *ESR1*

605 mutant clones exhibit a higher degree of heterogeneity. This is also supported by
606 clinical data: the recent BOLERO2 trial showed significant differences in overall survival
607 and everolimus response between Y537S and D538G mutations (9), and results from
608 the recent PALOMA3 trial suggest a potential Palbociclib resistance uniquely gained in
609 tumors bearing the Y537S mutation (60). Taken together, these proof-of-concept
610 studies are setting the stage for a more contextual and personalized therapeutic
611 targeting strategy in *ESR1* mutant breast cancer.

612 Of note, our comprehensive clinical investigation from four different cohorts (>900
613 samples) suggest that *ESR1* mutations are uncommon in local recurrences. The
614 significant exclusion of *ESR1* mutations in local recurrences is likely due to that *ESR1*
615 mutant clones are more equipped to escape from local-regional microenvironment. A
616 recently published study identified hotspot *ESR1* mutations in 15 out of 41 (36%) of
617 local-regional ER+ recurrences albeit at significantly lower mutation allele frequencies
618 (61). The reasons for this discrepancy are not clear, and future efforts are warranted to
619 explore details of potential differences in clinic-pathological features of the cohorts, and
620 technical approaches.

621 Lastly, we also sought to address the ER regulatory mechanisms involved in induction
622 of candidate metastatic driver genes utilizing ChIP-seq technology. Interestingly, none
623 of the metastatic candidate genes in *ESR1* mutant cells gained proximal ER binding
624 sites. This could be a result of our stringent hormone deprivation protocol resulting in
625 depletion of weaker binding events, and thus less sensitive binding site readouts (62).
626 This idea is supported by ChIP-seq data from Harrod et al. (28), which shows stronger
627 ER binding sites around *DSC2*, *DSG2* and *TIMP3* gene loci in MCF7-Y537S cells. Our
628 data, however, clearly shows that ER mutant cells display changes in indirect gene
629 regulation, resulting in metastatic phenotypes. This observation is due to non-canonical
630 ER action on chromatin structure remodeling, which was alternatively validated from our
631 ATAC-seq and FOXA1 ChIP-seq data. We propose that mutant ER reprograms FOXA1,
632 resulting in redistribution of FOXA1 binding to specific enhancers controlling the key
633 migratory driver gene(s). In addition, several recent studies uncovered the promising
634 role of androgen receptor (AR) in *ESR1* mutant tumors and cell models (18,63,64), and

635 additional studies are warranted to study *de novo* interplay between FOXA1, AR and
636 mutant ER.

637 Overall, our study serves as a timely and important preclinical report uncovering
638 mechanistic insights into *ESR1* mutations that can pave the way towards personalized
639 treatment of patients with advanced metastatic breast cancer.

640

641 **Acknowledgement**

642 We are grateful for advice, discussions and technical support from Dr. Ye Qin, Dr. Yu
643 Jiang, Dr. Min Yu, Yonatan Amzaleg and Meghan S. Mooring. We would like to thank Dr.
644 Peilu Wang for her contribution to earlier studies in the Lee-Oesterreich group on *ESR1*
645 mutations. This project used the University of Pittsburgh HSCRF Genomics Research
646 Core, the University of Pittsburgh Center for Research Computing, and the UPMC
647 Hillman Cancer Center Tissue and Research Pathology Services supported in part by
648 NIH grant award P30CA047904. The authors would like to thank the patients who
649 contributed samples to the tissue bank as well as all the clinicians and staff for their
650 efforts in collecting tissues.

651

652 **Funding**

653 This work was supported by the Breast Cancer Research Foundation (AVL, BHP and
654 SO]; Susan G. Komen Scholar awards (SAC110021 to AVL, SAC170078 to BHP,
655 SAC160073 to SO]; the Metastatic Breast Cancer Network Foundation [SO]; the
656 National Cancer Institute (R01CA221303 to SO, F30CA203154 to KML, F30CA250167
657 to MEY]; Department of Defense Breast Cancer Research Program (W81XWH1910434
658 to JG and W81XWH1910499 to SO), and the Fashion Footwear Association of New
659 York, Magee-Women's Research Institute and Foundation, The Canney Foundation,
660 The M&E Foundation, Nicole Meloche Foundation, Penguins Alumni Foundation, the
661 Pennsylvania Breast Cancer Coalition and the Shear Family Foundation. SO and AVL
662 are Hillman Fellows. ZL is supported by John S. Lazo Cancer Pharmacology Fellowship.
663 NT was supported by a Department of Defense Breakthrough Fellowship Award
664 [BC160764] and an NIH Pathway to Independence Award [K99CA237736]. This project
665 used the UPMC Hillman Cancer Center Tissue and Research Pathology Services
666 supported in part by NIH grant award P30CA047904.

667

668 **Conflict of Interest Disclosures**

669 SO and AVL receive research support from AstraZeneca PLC. AVL is employee and
670 consultant with UPMC Enterprises, and member of the Scientific Advisory Board,

671 Stockholder and receives compensation from Ocean Genomics. Tsinghua University
672 paid the stipend of University of Pittsburgh-affiliated foreign scholar Yang Wu from
673 Tsinghua University. MC serves for Pfizer (research support, honoraria), Lilly (advisor,
674 honoraria); Foundation Medicine (honoraria); Sermonix (advisor), G1Therapeutics
675 (advisor) and CytoDyn (advisor). LG receives travel expenses from Menarini SB. BHP
676 has ownership interest and is a paid member of the scientific advisory board of Loxo
677 Oncology and is a paid consultant for Foundation Medicine, Inc, Jackson Labs, Roche,
678 Eli Lilly, Casdin Capital, Astra Zeneca and H3 Biomedicine, and has research funding
679 from Abbvie, Pfizer and Foundation Medicine, Inc. Under separate licensing
680 agreements between Horizon Discovery, LTD and The Johns Hopkins University, BHP
681 is entitled to a share of royalties received by the University on sales of products. The
682 terms of this arrangement are being managed by The Johns Hopkins University in
683 accordance with its conflict-of-interest policies. CD reports grants from European
684 Commission H2020, grants from German Cancer Aid Translational Oncology, during
685 the conduct of the study; personal fees from Novartis, personal fees from Roche,
686 personal fees from MSD Oncology, personal fees from Daiichi Sankyo, personal fees
687 from AstraZeneca, from Molecular Health, grants from Myriad, personal fees from
688 Merck, other from Sividon diagnostics, outside the submitted work. In addition, CD has
689 a patent VMScope digital pathology software with royalties paid, a patent
690 WO2020109570A1 - cancer immunotherapy pending, and a patent WO2015114146A1
691 and WO2010076322A1- therapy response issued. PJ reports other support from
692 Myriad Genetics, Inc. which is outside the submitted work.
693

694 **Materials and methods**

695 Additional details are provided in the Supplementary Materials and Methods section.

696

697 **Human tissue studies from the Womens Cancer Research Center (WCRC) and**
698 **Charite cohorts**

699 All patients enrolled were approved within IRB protocols (PRO15050502) from the
700 University of Pittsburgh and Charite Universitaetsmedizin Berlin. Informed consent was
701 obtained from all participating patients. Biopsies were obtained and divided into distant
702 metastatic or local recurrent tumors. Genomic DNA was isolated from formalin fixed
703 paraffin embedded (FFPE) samples and *ESR1* mutation status was detected with
704 droplet digital PCR (ddPCR) targeting Y537S/C/N and D538G mutations in pre-
705 amplified *ESR1* LBD products as previously reported (7).

706 For the 54 ER+ metastatic tumor samples, genomic profiles were determined based on
707 tumor RNA sequencing provided in previous publications (25,26,65).

708

709 **CTCs analysis from the NU16B06 Cohort**

710 A retrospective cohort comprising 151 Metastatic Breast Cancer (BC) patients
711 characterized for CTCs, and ctDNA at the Robert H. Lurie Comprehensive Cancer
712 Center of Northwestern University (Chicago, IL) between 2015 and 2019 was analyzed.
713 Patients' enrollment was performed under the Investigator Initiated Trial (IIT) NU16B06
714 independently from treatment line. The overall baseline staging was performed
715 according to the investigators' choice, CTCs and ctDNA collection was performed prior
716 to treatment start. CTC enumeration was performed though the CellSearch™
717 immunomagnetic System (Menarini Silicon Biosystems). Mutations in *ESR1* (hotspots
718 D538 and Y537) and PIK3CA (hotspots E453 and H1047) were detected by either
719 ddPCR assay using the QX200 ddPCR System (Bio-Rad) or through the
720 Guardant360™ high sensitivity next-generation sequencing platform (Guardant Health,
721 CA). More details for CTC enumeration, mutation detection and statistical analysis can
722 be found in Supplementary Materials and Methods.

723

724 **Cell culture**

725 Genome-edited MCF7 and T47D *ESR1* mutant cell models from different sources were
726 maintained as previously described (12,19,28). Hormone deprivation was performed for
727 all experiments, unless otherwise stated. Other parental cell lines, ZR75-1 (CRL-1500),
728 MDA-MB-134-VI (HTB-23), MDA-MB-330 (HTB-127) and MDA-MB-468 (HTB-132),
729 were obtained from ATCC. BCK4 cells were developed as previously reported (66).

730

731 **Reagents**

732 17 β -estradiol (E2, #E8875) was obtained from Sigma, and Fulvestrant (#1047),
733 carbenoxolone disodium (#3096) and EDTA (#2811) were purchased from Tocris.
734 LGK974 (#14072) and T-5224 (#22904) were purchased from Cayman. Marimastat
735 (S7156) was obtained from SelleckChem. Recombinant human Wnt3A (5036-WN-010)
736 was purchased from R&D Systems. For knockdown experiments, siRNA against
737 *FOXA1* (#M-010319), *DSC1* (#L-011995), *DSC2* (#L-011996), *GJA1* (#L-011042) and
738 *GJB2* (#L-019285) were obtained from Horizon Discovery. Desmosome and scramble
739 peptides were designed based on previous studies (67,68) and synthesized from
740 GeneScript. Peptide sequences are presented in Supplementary Table S10.

741

742 **Animal Studies**

743 **Long term metastatic evaluation:** 4-week old female *nu/nu* athymic mice were
744 ordered from The Jackson Laboratory (002019 NU/J) according to University of
745 Pittsburgh IACUC approved protocol #19095822. MCF7 and T47D *ESR1* mutant cells
746 were hormone deprived and resuspended in PBS with a final concentration of 10⁷
747 cells/ml. 100 μ l of cell suspension was then injected via tail vein into nude mice with 7
748 mice per group. Mice were under observation weekly. According to the IACUC protocol,
749 if greater than 50% of mice in any group show predefined signs of euthanasia, the entire
750 cohort needs to be euthanized. Cohorts were euthanized at 13 weeks for MCF7 cell-
751 injected mice and 23 weeks for T47D cell-injected mice. Macro-metastatic tumors and
752 potential organs (lung, liver, UG tract) for metastatic spread were harvested. Solid
753 macro-metastatic tumors (non-lymph node) were counted for comparison. All tissues
754 were processed for FFPE preparation and hematoxylin and eosin (H&E) staining by the
755 Histology Core at Magee Women's Research Institute. Macro-metastatic tumor FFPE

756 sections were further evaluated by a trained pathologist. Micro-metastatic lesions in the
757 lung were further examined and quantified by immunofluorescence staining as
758 described in supplementary materials and methods.

759 **Short term CTC cluster assessment:** 4-week old female *nu/nu* athymic mice were
760 ordered from The Jackson Laboratory (002019 NU/J) according to University of
761 Pittsburgh IACUC approved protocol #19095822. MCF7 WT and mutant cells were
762 stably labelled with RFP-luciferase by infection with the pLEX-TRC210/L2N-TurboRFP-
763 c lentivirus plasmid. Labelled cells were hormone deprived and resuspended in PBS at
764 a final concentration of 10^7 cells/ml. 100 μ l of cell suspension was then injected into
765 nude mice with 6 mice per group via an intracardiac left ventricle injection. Post-injected
766 mice were immediately imaged using the IVIS200 *in vivo* imaging system (124262,
767 PerkinElmer) after D-luciferin intraperitoneal injection to confirm successful cell delivery
768 into the circulation system. All mice were euthanized after one hour of injection and their
769 whole blood were extracted via cardiac puncture and collected into CellSave
770 Preservative Tubes (#790005, CellSearch). Blood samples were mixed with 7ml of
771 RPMI media and shipped to University of Minnesota for CTC enrichment. CTCs were
772 extracted using an electric size-based microfilter system (FaCTChekr) and stained with
773 antibody against pan-cytokeratins (CK) and DAPI. Slides with stained CTCs were
774 manually scanned in a blind manner and all visible single CTCs or clusters were imaged
775 under 5X or 40X magnification respectively. To set up criteria for identifying CTC
776 clusters via images, we analyzed seven single CTCs with intact CK signal distribution
777 and calculated the average nuclei-edge to membrane distance (x). Inter-nuclei-edge
778 distance greater than 2x for any two CTCs were excluded in CTC cluster calling. All
779 measurements were performed in a blind manner. Details of filter and staining are
780 included in the supplementary materials and methods.

781

782 **qRT-PCR**

783 MCF7 and T47D cells were seeded in triplicates into 6-well plates with 120,000 and
784 90,000 cells per well respectively. After desired treatments, RNA was and cDNA was
785 synthesized using iScript kit (#1708890, BioRad, Hercules, CA). qRT-PCR reactions
786 were performed with SybrGreen Supermix (#1726275, BioRad), and the $\Delta\Delta Ct$ method

787 was used to analyze relative mRNA fold changes with *RPLP0* measurements serving as
788 the internal control. All primer sequences can be found in Supplementary Table S10.

789

790 **Immunoblotting**

791 After desired treatments, cells were lysed with RIPA buffer spiked with a fresh protease
792 and phosphatase cocktail (Thermo Scientific, #78442) and sonicated. Protein
793 concentrations were quantified using the Pierce BCA assay kit (Thermo Fisher, #23225).
794 80-120µg of protein for each sample was loaded onto SDS-PAGE gels, and then
795 transferred onto PVDF membranes. The blots were incubated with the following
796 antibodies: desmocollin 1 (sc-398590), desmoglein 2 (sc-80663), plakophilin (sc-33636),
797 connexin 26 (sc-7261) and cFOS (sc-52) from Santa Cruz; ER- α (#8644), HA (#3724),
798 Non-phospho- β -catenin (#19807), Histone H3 (#4499), AIF (#5318), GSK3 β (Ser9,
799 #5558), phospho-GSK3 α (Ser21, #9316), GSK3 β (#12456) and GSK3 α (#4337) from
800 Cell Signaling Technology; β -catenin (#610154) from BD; Tubulin (T6557) and connexin
801 43 (C6219) from Sigma Aldrich; and *TIMP3* (ab39184) from Abcam.

802

803 **IncuCyte Live Cell Imaging System**

804 *Wound scratch assay.* MCF7 or T47D cells were seeded at 150,000 cells/well into
805 Imagelock 96-well plates (Essen Bioscience, #4379) pre-coated with Matrigel (Corning,
806 #356237). Wounds were scratched in the middle of each well using a Wound Maker
807 (Essen Bioscience, #4493). Desired treatments mixed with 5µg/ml of proliferation
808 blocker Mitomycin C (Sigma-Aldrich, #10107409001) were loaded after two washes with
809 PBS. The IncuCyte Zoom system was used to record wound images every 4 hours and
810 wound closure density was calculated using the manufacturer's wound scratch assay
811 module. For the dominant negative *TCF4* overexpression experiment, Myc-tagged
812 DN*TCF4* plasmids (Addgene, #32729) were transiently transfected into targeted cells
813 for a total of 24 hours before being subjected to the wound scratch assay.

814 *Aggregation rate assay.* 3,000 MCF7 or 4,000 T47D cells were seeded into 96-well
815 round bottom ultra-low attachment plates (Corning, #7007) with 100µl of respective
816 media in each well. Cell aggregation was monitored by the IncuCyte living imaging
817 system every hour. Spheroid areas were normalized to time 0.

818

819 **Calcein-labelled cell-cell interaction assay**

820 MCF7 and T47D cells were seeded into black-walled 96 well plate at 15,000 cells per
821 well to achieve a fully confluent monolayer after 24 hours. Separate cultures of cells
822 were digested and labelled with 1 μ M calcein AM (BD Pharmingen, #564061) for 30
823 minutes in room temperature. 40,000 labelled cells were loaded on top of the previously
824 plated monolayers and incubated for 1 hour at 37°C. Cells were washed three times
825 after incubation by manually pouring out the PBS washing agent. The plates were read
826 using Victor X4 plate reader (PerkinElmer) under the excitation and emission
827 wavelength of 485/535nm. Cell-cell adhesion ratios were calculated by dividing the
828 post-wash readouts to the pre-wash readouts after each wash. For the vacuum
829 aspiration method, we used a standard laboratory vacuum pump with a modified speed
830 of approximately 100 ml/minutes. Adhesion ratios after three washes were plotted
831 separately for each independent experiment.

832

833 **Ibidi microfluidic system**

834 MCF7 and T47D *ESR1* mutant cells were hormone deprived for 3 days and diluted to
835 10⁶ cells in 14ml of respective media before being loaded into the ibidi pump system
836 (ibidi, #10902). Cells were constantly flowing with 15dynes/cm of shear stress for two
837 hours before immediate imaging after being seeded back into a flat bottom ULA plate.
838 For each group, six wells were imaged twice. Time zero (T0) cells were also imaged as
839 the initial time point control. Cell numbers in clusters or non-clusters were manually
840 counted. Cell cluster ratios were calculated by dividing the cell numbers in clusters to
841 the total number of cells. Cell clustering grade was calculated by the cell numbers
842 present in each cluster. For CBX treatment, cells were pre-treated with 100 μ M CBX for
843 two days before being added to the flow chamber. For the desmosome blocking
844 peptides treatment, 75 μ M of each *DSC1*, *DSC2*, *DSG1* and *DSG2* peptide or 150 μ M of
845 each scramble peptide were pre-mixed into cell suspension for flow experiments.

846

847 **Cell-ECM adhesion assay**

848 30,000 cells/well were seeded into collagen I coated (Thermo Fisher Scientific,
849 A1142803) or uncoated 96-well plates. For the ECM array assay, cells were
850 resuspended and loaded into the ECM array plate (EMD Millipore, ECM540). After a 2-
851 hour incubation at 37°C, the plates were washed with PBS three times, and attached
852 cells were quantified using the FluoReporter kit (Thermo Fisher Scientific, F2962).
853 Adhesion ratios were calculated by dividing the remaining cell counts in the washed
854 wells to the initial cell counts in pre-washed plates. For *TIMP3* overexpression, the
855 PRK5M-*TIMP3* plasmid (Addgene, #31715) was transfected into targeted cells, which
856 was subjected to the adhesion assay after a 24-hour transfection period.

857

858 **Chromatin-immunoprecipitation (ChIP)**

859 ChIP experimentation was performed as previously described (39). The
860 immunoprecipitation was performed using ERα (sc543) and rabbit IgG (sc2027)
861 antibodies (Santa Cruz Biotechnologies). Histone 3 acetylation at K27 site (ab4739),
862 and Histone 3 di-methylation at K4 site (ab7766) and FOXA1 (ab23738) antibodies
863 were obtained from Abcam.

864

865 **ChIP-sequencing Analysis**

866 ChIP-seq reads were aligned to Hg19 reference genome assembly using Bowtie 2.0
867 (69), and peaks were called using MACS2.0 with a p-value<10⁻⁵ (ER ChIP-seq) or a q-
868 value<0.05 (FOXA1 ChIP-seq) (70). We used the Diffbind package (71) to perform
869 principle component analysis, identify differentially bound regions and analyze
870 intersection ratios with other datasets. Briefly, all BED files for each cell line were
871 merged and binding intensity was estimated at each site based on the normalized read
872 counts in the BAM files. Pairwise comparisons between WT and mutant samples were
873 performed to calculate fold change (FC). Binding sites were sub-classified into three
874 categories: gained sites (FC>2), lost sites (FC<-2), and not-changed sites (2<FC<2).
875 Heatmaps and intensity plots for binding peaks were visualized by EaSeq (72). For
876 gene annotation from FOXA1 binding sites, gained FOXA1 peaks were selected and
877 annotated genes were inspected in a ± 200kb range of the FOXA1 peaks using
878 ChIPseeker (73). For intersection analysis of the D538G-regulated non-canonical

879 ligand-independent genes, broad differentially expressing genes were first called using
880 a cutoff of $|fold\ change| > 2$, $FDR < 0.005$ between WT and D538G cells. Meanwhile, E2-
881 regulated genes were called using the cutoff of $|fold\ change| > 1.5$, $FDR < 0.01$ between
882 WT and WT+E2 groups. D538G ligand-independent genes which are also regulated in
883 WT cells were excluded from the analysis.

884

885 **RNA-sequencing analysis**

886 Data generation and processing of the 54 ER+ tumors in the WCRC cohort was
887 described above. For the MET500 cohort, RNA-seq fastq files from 91 metastatic breast
888 cancer samples were downloaded from the Database of Genotypes and Phenotypes
889 (dbGaP) with accession number phs000673.v2.p1. Transcript counts from all samples
890 were quantified with Salmon v.0.8.2 and converted to gene-level counts with tximport.
891 The gene-level counts from all studies were then normalized together using TMM with
892 edgeR. Log2 transformed TMM-normalized counts per million [$\log_2(TMM-CPM+1)$] were
893 used for analysis. 46 putative ER positive samples were then filtered in the MET500
894 cohort. *ESR1* mutation status was extracted using the MET500 portal
895 (<https://met500.path.med.umich.edu>). For the DFCI cohort, raw counts data was
896 obtained and normalized to $\log_2(TMM-CPM+1)$ for further analysis. *ESR1* mutation
897 status was called using separate whole exon sequencing data. For the POG570 cohort,
898 raw count matrixes and mutation statuses were downloaded from the BCGSC portal
899 (<https://www.bcgsc.ca/downloads/POG570/>). ER status of each patient was additionally
900 requested from the cited original resources and only ER+ metastatic tumors were used
901 for downstream analysis.

902 For all datasets, differential expression (DE) analysis was performed using the DESeq2
903 package (74). In brief, genes were prefiltered with a $\log_2(CPM+1) > 1$ in at least one
904 sample criteria across all data sets. DE genes with a q-value below 0.1 and an absolute
905 \log_2 fold change above 1.5 were used for Ingenuity Pathway Analysis (75). GSEA
906 analysis was performed using the Broad GSEA Application (76). Gene set variation
907 analyses were performed using the GSVA package (77). All gene sets used in this
908 study are reported in Supplementary Table S6. Data visualizations were performed
909 using “ggpubr” (78) and “VennDiagram” packages (79).

910

911 **Statistical Analysis**

912 GraphPad Prism software version 7 and R version 3.6.1 were used for statistical
913 analysis. All experimental results included biological replicates and were shown as
914 mean \pm standard deviation, unless otherwise stated. Specific statistical tests were
915 indicated in corresponding figure legends. All tests were conducted as two-tailed, with a
916 $p < 0.05$ considered statistically significant. Drug synergy was calculated based on the
917 Bliss independence model using the SynergyFinder (<https://synergyfinder.fimm.fi/>) (80).
918 Bliss synergy scores were used to determine synergistic effects.

919

920 **Data Availability**

921 The ER and FOXA1 ChIP-seq data has been deposited onto the Gene Expression
922 Omnibus database (GSE125117 and GSE165280). All publicly available resources
923 used in this study are summarized in Supplementary Table S11. All raw data and scripts
924 are available upon request from the corresponding author.

925

926 **Reference**

- 927 1. DeSantis CE, Ma J, Goding Sauer A, Newman LA, Jemal A. Breast cancer statistics, 2017, racial
928 disparity in mortality by state. *CA: a cancer journal for clinicians* **2017**;67(6):439-48.
- 929 2. Turner NC, Neven P, Loibl S, Andre F. Advances in the treatment of advanced oestrogen-
930 receptor-positive breast cancer. *The Lancet* **2017**;389(10087):2403-14.
- 931 3. Spoerke JM, Gendreau S, Walter K, Qiu J, Wilson TR, Savage H, *et al.* Heterogeneity and clinical
932 significance of ESR1 mutations in ER-positive metastatic breast cancer patients receiving
933 fulvestrant. *Nature communications* **2016**;7:11579.
- 934 4. Robinson DR, Wu Y-M, Vats P, Su F, Lonigro RJ, Cao X, *et al.* Activating ESR1 mutations in
935 hormone-resistant metastatic breast cancer. *Nature genetics* **2013**;45(12):1446-51.
- 936 5. Toy W, Weir H, Razavi P, Lawson M, Goeppert AU, Mazzola AM, *et al.* Activating ESR1 Mutations
937 Differentially Affect the Efficacy of ER Antagonists. *Cancer discovery* **2017**;7(3):277-87.
- 938 6. Schiavon G, Hrebien S, Garcia-Murillas I, Cutts RJ, Pearson A, Tarazona N, *et al.* Analysis of ESR1
939 mutation in circulating tumor DNA demonstrates evolution during therapy for metastatic breast
940 cancer. *Science translational medicine* **2015**;7(313):313ra182-313ra182.
- 941 7. Wang P, Bahreini A, Gyanchandani R, Lucas PC, Hartmaier RJ, Watters RJ, *et al.* Sensitive
942 detection of mono-and polyclonal ESR1 mutations in primary tumors, metastatic lesions, and
943 cell-free DNA of breast cancer patients. *Clinical cancer research* **2016**;22(5):1130-7.
- 944 8. Zhang K, Hong R, Xu F, Xia W, Kaping L, Qin G, *et al.* Clinical value of circulating ESR1 mutations
945 for patients with metastatic breast cancer: a meta-analysis. *Cancer management and research*
946 **2018**;10:2573.
- 947 9. Chandarlapaty S, Chen D, He W, Sung P, Samoila A, You D, *et al.* Prevalence of ESR1 mutations in
948 cell-free DNA and outcomes in metastatic breast cancer: a secondary analysis of the BOLERO-2
949 clinical trial. *JAMA oncology* **2016**;2(10):1310-5.
- 950 10. Toy W, Shen Y, Won H, Green B, Sakr RA, Will M, *et al.* ESR1 ligand-binding domain mutations in
951 hormone-resistant breast cancer. *Nature genetics* **2013**;45(12):1439-45.
- 952 11. Harrod A, Fulton J, Nguyen VT, Periyasamy M, Ramos-Garcia L, Lai C-F, *et al.* Genomic modelling
953 of the ESR1 Y537S mutation for evaluating function and new therapeutic approaches for
954 metastatic breast cancer. *Oncogene* **2017**;36(16):2286.
- 955 12. Bahreini A, Li Z, Wang P, Levine KM, Tasdemir N, Cao L, *et al.* Mutation site and context
956 dependent effects of ESR1 mutation in genome-edited breast cancer cell models. *Breast Cancer
957 Research* **2017**;19(1):60.
- 958 13. Fanning SW, Mayne CG, Dharmarajan V, Carlson KE, Martin TA, Novick SJ, *et al.* Estrogen
959 receptor alpha somatic mutations Y537S and D538G confer breast cancer endocrine resistance
960 by stabilizing the activating function-2 binding conformation. *Elife* **2016**;5.
- 961 14. Jeselsohn R, Bergholz JS, Pun M, Cornwell M, Liu W, Nardone A, *et al.* Allele-specific chromatin
962 recruitment and therapeutic vulnerabilities of ESR1 activating mutations. *Cancer cell*
963 **2018**;33(2):173-86. e5.
- 964 15. Yu L, Wang L, Mao C, Duraki D, Kim JE, Huang R, *et al.* Estrogen-Independent Myc
965 Overexpression Confers Endocrine Therapy Resistance on Breast Cancer Cells Expressing
966 ER α Y537S and ER α D538G Mutations. *Cancer letters* **2018**.
- 967 16. Merenbakh-Lamin K, Ben-Baruch N, Yeheskel A, Dvir A, Soussan-Gutman L, Jeselsohn R, *et al.*
968 D538G mutation in estrogen receptor- α : A novel mechanism for acquired endocrine resistance
969 in breast cancer. *Cancer research* **2013**;73(23):6856-64.
- 970 17. Gelsomino L, Gu G, Rechoum Y, Beyer AR, Pejerrey SM, Tsimelzon A, *et al.* ESR1 mutations affect
971 anti-proliferative responses to tamoxifen through enhanced cross-talk with IGF signaling. *Breast
972 cancer research and treatment* **2016**;157(2):253-65.

973 18. Gu G, Tian L, Herzog SK, Rechoum Y, Gelsomino L, Gao M, *et al.* Hormonal modulation of ESR1
974 mutant metastasis. *Oncogene* **2020**:1-15.

975 19. Arnesen S, Blanchard Z, Williams MM, Berrett KC, Li Z, Oesterreich S, *et al.* Estrogen receptor
976 alpha mutations in breast cancer cells cause gene expression changes through constant activity
977 and secondary effects. *Cancer Research* **2020**:canres.1171.2020 doi 10.1158/0008-5472.Can-20-
978 1171.

979 20. Razavi P, Chang MT, Xu G, Bandlamudi C, Ross DS, Vasan N, *et al.* The Genomic Landscape of
980 Endocrine-Resistant Advanced Breast Cancers. *Cancer cell* **2018**;34(3):427-38. e6.

981 21. Paul MR, Pan T-c, Pant DK, Shih NN, Chen Y, Harvey KL, *et al.* Genomic landscape of metastatic
982 breast cancer identifies preferentially dysregulated pathways and targets. *The Journal of Clinical
983 Investigation* **2020**;130(8).

984 22. Pleasance E, Titmuss E, Williamson L, Kwan H, Culibrk L, Zhao EY, *et al.* Pan-cancer analysis of
985 advanced patient tumors reveals interactions between therapy and genomic landscapes. *Nature
986 Cancer* **2020**;1(4):452-68.

987 23. Fumagalli C, Ranghiero A, Gandini S, Corso F, Taormina S, De Camilli E, *et al.* Inter-tumor
988 genomic heterogeneity of breast cancers: comprehensive genomic profile of primary early
989 breast cancers and relapses. *Breast Cancer Research* **2020**;22(1):1-11.

990 24. Priedigkeit N, Hartmaier RJ, Chen Y, Vareslija D, Basudan A, Watters RJ, *et al.* Intrinsic subtype
991 switching and acquired ERBB2/HER2 amplifications and mutations in breast cancer brain
992 metastases. *JAMA oncology* **2017**;3(5):666-71.

993 25. Priedigkeit N, Watters RJ, Lucas PC, Basudan A, Bhargava R, Horne W, *et al.* Exome-capture RNA
994 sequencing of decade-old breast cancers and matched decalcified bone metastases. *JCI insight*
995 **2017**;2(17).

996 26. Levine KM, Priedigkeit N, Basudan A, Tasdemir N, Sikora MJ, Sokol ES, *et al.* FGFR4
997 overexpression and hotspot mutations in metastatic ER+ breast cancer are enriched in the
998 lobular subtype. *NPJ breast cancer* **2019**;5(1):1-5.

999 27. Robinson DR, Wu Y-M, Lonigro RJ, Vats P, Cobain E, Everett J, *et al.* Integrative clinical genomics
1000 of metastatic cancer. *Nature* **2017**;548(7667):297.

1001 28. Harrod A, Fulton J, Nguyen VT, Periyasamy M, Ramos-Garcia L, Lai C-F, *et al.* Genomic modelling
1002 of the ESR1 Y537S mutation for evaluating function and new therapeutic approaches for
1003 metastatic breast cancer. *Oncogene* **2016**.

1004 29. Jia S, Miedel MT, Ngo M, Hessenius R, Chen N, Wang P, *et al.* Clinically Observed Estrogen
1005 Receptor Alpha Mutations within the Ligand-Binding Domain Confer Distinguishable Phenotypes.
1006 *Oncology* **2018**;94(3):176-89.

1007 30. Aceto N, Bardia A, Miyamoto DT, Donaldson MC, Wittner BS, Spencer JA, *et al.* Circulating tumor
1008 cell clusters are oligoclonal precursors of breast cancer metastasis. *Cell* **2014**;158(5):1110-22.

1009 31. Ungefroren H, Sebens S, Seidl D, Lehnert H, Hass R. Interaction of tumor cells with the
1010 microenvironment. *Cell Communication and Signaling* **2011**;9(1):18.

1011 32. Friedl P, Locker J, Sahai E, Segall JE. Classifying collective cancer cell invasion. *Nature cell biology*
1012 **2012**;14(8):777.

1013 33. Jimenez MA, Tutuncuoglu E, Barge S, Novelli EM, Sundd P. Quantitative microfluidic
1014 fluorescence microscopy to study vaso-occlusion in sickle cell disease. *haematologica*
1015 **2015**;100(10):e390-e3.

1016 34. Ao Z, Shah SH, Machlin LM, Parajuli R, Miller PC, Rawal S, *et al.* Identification of cancer-
1017 associated fibroblasts in circulating blood from patients with metastatic breast cancer. *Cancer
1018 research* **2015**;75(22):4681-7.

1019 35. Tasdemir N, Bossart EA, Li Z, Zhu L, Sikora MJ, Levine KM, et al. Comprehensive phenotypic
1020 characterization of human invasive lobular carcinoma cell lines in 2D and 3D cultures. *Cancer*
1021 research **2018**;78(21):6209-22.

1022 36. Cunha S, Lin Y-C, Goossen EA, DeVette CI, Albertella MR, Thomson S, et al. The RON receptor
1023 tyrosine kinase promotes metastasis by triggering MBD4-dependent DNA methylation
1024 reprogramming. *Cell reports* **2014**;6(1):141-54.

1025 37. Gkountela S, Castro-Giner F, Szczerba BM, Vetter M, Landin J, Scherrer R, et al. Circulating tumor
1026 cell clustering shapes DNA methylation to enable metastasis seeding. *Cell* **2019**;176(1-2):98-112.
1027 e14.

1028 38. Yu M, Bardia A, Aceto N, Bersani F, Madden MW, Donaldson MC, et al. Ex vivo culture of
1029 circulating breast tumor cells for individualized testing of drug susceptibility. *Science*
1030 **2014**;345(6193):216-20.

1031 39. Sikora MJ, Cooper KL, Bahreini A, Luthra S, Wang G, Chandran UR, et al. Invasive lobular
1032 carcinoma cell lines are characterized by unique estrogen-mediated gene expression patterns
1033 and altered tamoxifen response. *Cancer research* **2014**:canres. 2779.013.

1034 40. Need EF, Selth LA, Harris TJ, Birrell SN, Tilley WD, Buchanan G. Research resource: interplay
1035 between the genomic and transcriptional networks of androgen receptor and estrogen receptor
1036 α in luminal breast cancer cells. *Molecular endocrinology* **2012**;26(11):1941-52.

1037 41. Creighton CJ, Cordero KE, Larios JM, Miller RS, Johnson MD, Chinnaiyan AM, et al. Genes
1038 regulated by estrogen in breast tumor cells in vitro are similarly regulated in vivo in tumor
1039 xenografts and human breast tumors. *Genome biology* **2006**;7(4):R28.

1040 42. Li Z, Wu Y, Bahreini A, Priedigkeit NM, Ding K, Sartorius CA, et al. ESR1 mutant breast cancers
1041 show elevated basal cytokeratins and immune activation. *bioRxiv* **2020**.

1042 43. Oyamada M, Takebe K, Oyamada Y. Regulation of connexin expression by transcription factors
1043 and epigenetic mechanisms. *Biochimica et Biophysica Acta (BBA)-Biomembranes*
1044 **2013**;1828(1):118-33.

1045 44. Nigam A, Savage F, Boulos P, Stamp G, Liu D, Pignatelli M. Loss of cell-cell and cell-matrix
1046 adhesion molecules in colorectal cancer. *British journal of cancer* **1993**;68(3):507.

1047 45. Rege TA, Haggard JS. Thy-1 as a regulator of cell-cell and cell-matrix interactions in axon
1048 regeneration, apoptosis, adhesion, migration, cancer, and fibrosis. *The FASEB journal*
1049 **2006**;20(8):1045-54.

1050 46. Anania M, Sensi M, Radaelli E, Miranda C, Vizioli M, Pagliardini S, et al. TIMP3 regulates
1051 migration, invasion and in vivo tumorigenicity of thyroid tumor cells. *Oncogene*
1052 **2011**;30(27):3011-23.

1053 47. Su C-W, Chang Y-C, Chien M-H, Hsieh Y-H, Chen M-K, Lin C-W, et al. Loss of TIMP3 by promoter
1054 methylation of Sp1 binding site promotes oral cancer metastasis. *Cell death & disease*
1055 **2019**;10(11):1-17.

1056 48. Anania M, Sensi M, Radaelli E, Miranda C, Vizioli M, Pagliardini S, et al. TIMP3 regulates
1057 migration, invasion and in vivo tumorigenicity of thyroid tumor cells. *Oncogene*
1058 **2011**;30(27):3011.

1059 49. Zardavas D, Baselga J, Piccart M. Emerging targeted agents in metastatic breast cancer. *Nature*
1060 *reviews Clinical oncology* **2013**;10(4):191.

1061 50. Liu J, Pan S, Hsieh MH, Ng N, Sun F, Wang T, et al. Targeting Wnt-driven cancer through the
1062 inhibition of Porcupine by LGK974. *Proceedings of the National Academy of Sciences*
1063 **2013**;110(50):20224-9.

1064 51. Li Z, Levine KM, Bahreini A, Wang P, Chu D, Park BH, et al. Upregulation of IRS1 enhances IGF1
1065 response in Y537S and D538G ESR1 mutant breast cancer cells. *Endocrinology* **2017**;159(1):285-
1066 96.

1067 52. Davis AA, Zhang Q, Gerratana L, Shah AN, Zhan Y, Qiang W, *et al.* Association of a novel
1068 circulating tumor DNA next-generating sequencing platform with circulating tumor cells (CTCs)
1069 and CTC clusters in metastatic breast cancer. *Breast Cancer Research* **2019**;21(1):1-8.

1070 53. Gerratana L, Davis AA, Polano M, Zhang Q, Shah AN, Lin C, *et al.* Understanding the organ
1071 tropism of metastatic breast cancer through the combination of liquid biopsy tools. *European
1072 Journal of Cancer* **2021**;143:147-57.

1073 54. Cheung KJ, Gabrielson E, Werb Z, Ewald AJ. Collective invasion in breast cancer requires a
1074 conserved basal epithelial program. *Cell* **2013**;155(7):1639-51.

1075 55. Aasen T, Mesnil M, Naus CC, Lampe PD, Laird DW. Gap junctions and cancer: communicating for
1076 50 years. *Nature Reviews Cancer* **2016**;16(12):775.

1077 56. Xu X, Wang J, Han K, Li S, Xu F, Yang Y. Antimalarial drug mefloquine inhibits nuclear factor
1078 kappa B signaling and induces apoptosis in colorectal cancer cells. *Cancer science*
1079 **2018**;109(4):1220-9.

1080 57. Yulyana Y, Endaya BB, Ng WH, Guo CM, Hui KM, Lam PY, *et al.* Carbenoxolone enhances TRAIL-
1081 induced apoptosis through the upregulation of death receptor 5 and inhibition of gap junction
1082 intercellular communication in human glioma. *Stem cells and development* **2013**;22(13):1870-82.

1083 58. Mao C, Livezey M, Kim JE, Shapiro DJ. Antiestrogen Resistant Cell Lines Expressing Estrogen
1084 Receptor α Mutations Upregulate the Unfolded Protein Response and are Killed by BHPI.
1085 *Scientific Reports* **2016**;6.

1086 59. Simpson KJ, Selfors LM, Bui J, Reynolds A, Leake D, Khvorova A, *et al.* Identification of genes that
1087 regulate epithelial cell migration using an siRNA screening approach. *Nature cell biology*
1088 **2008**;10(9):1027.

1089 60. O'Leary B, Cutts RJ, Liu Y, Hrebien S, Huang X, Fenwick K, *et al.* The genetic landscape and clonal
1090 evolution of breast cancer resistance to palbociclib plus fulvestrant in the PALOMA-3 trial.
1091 *Cancer discovery* **2018**;8(11):1390-403.

1092 61. Zundelevich A, Dadiani M, Kahana-Edwin S, Itay A, Sella T, Gadot M, *et al.* ESR1 mutations are
1093 frequent in newly diagnosed metastatic and loco-regional recurrence of endocrine-treated
1094 breast cancer and carry worse prognosis. *Breast Cancer Research* **2020**;22(1):1-11.

1095 62. Sikora MJ, Johnson MD, Lee AV, Oesterreich S. Endocrine response phenotypes are altered by
1096 charcoal-stripped serum variability. *Endocrinology* **2016**;157(10):3760-6.

1097 63. Ponnusamy S, Asemota S, Schwartzberg LS, Guestini F, McNamara KM, Pierobon M, *et al.*
1098 Androgen receptor is a non-canonical inhibitor of wild-type and mutant estrogen receptors in
1099 hormone receptor-positive breast cancers. *Iscience* **2019**;21:341-58.

1100 64. Williams MM, Spoelstra NS, Arnesen S, O'Neill KI, Christenson JL, Reese J, *et al.* Steroid hormone
1101 receptor and infiltrating immune cell status reveals therapeutic vulnerabilities of ESR1 mutant
1102 breast cancer. *Cancer Research* **2020**.

1103 65. Varešlija D, Priedigkeit N, Fagan A, Purcell S, Cosgrove N, O'Halloran PJ, *et al.* Transcriptome
1104 characterization of matched primary breast and brain metastatic tumors to detect novel
1105 actionable targets. *JNCI: Journal of the National Cancer Institute* **2018**.

1106 66. Jambal P, Badtke MM, Harrell JC, Borges VF, Post MD, Sollender GE, *et al.* Estrogen switches
1107 pure mucinous breast cancer to invasive lobular carcinoma with mucinous features. *Breast
1108 cancer research and treatment* **2013**;137(2):431-48.

1109 67. Tselepis C, Chidgey M, North A, Garrod D. Desmosomal adhesion inhibits invasive behavior.
1110 *Proceedings of the National Academy of Sciences* **1998**;95(14):8064-9.

1111 68. Runswick SK, O'Hare MJ, Jones L, Streuli CH, Garrod DR. Desmosomal adhesion regulates
1112 epithelial morphogenesis and cell positioning. *Nature cell biology* **2001**;3(9):823-30.

1113 69. Langmead B. Aligning short sequencing reads with Bowtie. *Current protocols in bioinformatics*
1114 **2010**;32(1):11.7. 1-7. 4.

1115 70. Feng J, Liu T, Qin B, Zhang Y, Liu XS. Identifying ChIP-seq enrichment using MACS. *Nature*
1116 protocols **2012**;7(9):1728.

1117 71. Stark R, Brown G. DiffBind: differential binding analysis of ChIP-Seq peak data. R package version
1118 **2011**;100:4.3.

1119 72. Lerdrup M, Johansen JV, Agrawal-Singh S, Hansen K. An interactive environment for agile
1120 analysis and visualization of ChIP-sequencing data. *Nature structural & molecular biology*
1121 **2016**;23(4):349.

1122 73. Yu G, Wang L-G, He Q-Y. ChIPseeker: an R/Bioconductor package for ChIP peak annotation,
1123 comparison and visualization. *Bioinformatics* **2015**;31(14):2382-3.

1124 74. Love MI, Huber W, Anders S. Moderated estimation of fold change and dispersion for RNA-seq
1125 data with DESeq2. *Genome biology* **2014**;15(12):550.

1126 75. Krämer A, Green J, Pollard Jr J, Tugendreich S. Causal analysis approaches in ingenuity pathway
1127 analysis. *Bioinformatics* **2013**;30(4):523-30.

1128 76. Subramanian A, Tamayo P, Mootha VK, Mukherjee S, Ebert BL, Gillette MA, et al. Gene set
1129 enrichment analysis: a knowledge-based approach for interpreting genome-wide expression
1130 profiles. *Proceedings of the National Academy of Sciences* **2005**;102(43):15545-50.

1131 77. Hänzelmann S, Castelo R, Guinney J. GSVA: gene set variation analysis for microarray and RNA-
1132 seq data. *BMC bioinformatics* **2013**;14(1):7.

1133 78. Kassambara A. ggpubr: “ggplot2” based publication ready plots. R package version 01 **2017**;6.

1134 79. Chen H, Boutros PC. VennDiagram: a package for the generation of highly-customizable Venn
1135 and Euler diagrams in R. *BMC bioinformatics* **2011**;12(1):35.

1136 80. Ianevski A, He L, Aittokallio T, Tang J. SynergyFinder: a web application for analyzing drug
1137 combination dose-response matrix data. *Bioinformatics* **2017**;33(15):2413-5.

1138

1139

1140

Cohorts	Site of Recurrence	Total Number	ESR1 WT	ESR1 Mutant	Fisher's Exact p
METAMORPH/POG570/ MSKCC/IEO Merged	Distant	867	711 (82%)	158 (18%)	0.0014
	Local	38	38 (100%)	0 (0%)	
WCRC/Charite	Distant	48	36 (75%)	12 (25%)	0.0031
	Local	27	27 (100%)	0 (0%)	

1141 **Table**

1142

1143 **Table 1. Significant enrichment of *ESR1* mutations in distant compared to local**
1144 **recurrences.**

1145 Upper panel: Data from 867 distant metastatic and 38 local recurrence cases were
1146 merged from three cohorts (METAMORPH, 39 distant/9 local; POG570, 86 distant/14
1147 local; MSKCC, 716 distant/8 local; IEO, 26 distant/7 local). *ESR1* mutation status was
1148 previously identified by whole exome sequencing (METAMORPH), whole genome
1149 sequencing (POG570) or target panel DNA sequencing (MSKCC, IEO). Lower panel: 48
1150 distant ER positive metastases and 27 local ER positive recurrences were obtained
1151 from the WCRC and Charite cohorts. Genomic DNA (gDNA) was isolated from either
1152 FFPE or frozen tumor tissues, and subjected to droplet digital PCR (ddPCR) detection
1153 with specific probes against Y537S, Y537C, Y537N and D538G hotspot point mutations
1154 (cDNA rather than gDNA was used for 3 of the local recurrent samples). Hotspot *ESR1*
1155 mutation incidences between distant metastatic and local recurrent samples in both
1156 panels were compared using a Fisher's exact test.

1157

1158 **Figure legends**

1159

1160 **Figure 1. Transcriptomic landscape of *ESR1* mutant metastatic breast cancers.**

1161 A. Schematic overview of transcriptomic analysis of four ER+ metastatic breast cancer
1162 cohorts.

1163 B. Box plots representing the enrichment levels of “Estrogen Response Early” and
1164 “Estrogen Response Late” signatures in *ESR1* mutant versus *ESR1* WT metastatic
1165 tumors in each cohort. (WCRC, 46 *ESR1* WT/8 mutant; MET500, 34 *ESR1* WT/12
1166 *ESR1* mutant; DFCI, 98 *ESR1* WT/32 mutant; POG570, 68 *ESR1* WT/18 mutant). Four
1167 quantiles are shown in each plot. Mann-Whitney U test was used to compare the
1168 enrichment of the signatures in WT and mutant tumors. (* p<0.05, ** p<0.01)

1169 C. Volcano plots representing the differentially expressing genes (DE genes) in *ESR1*
1170 mutant tumors versus WT tumors in the three metastatic breast cancer cohorts. DE
1171 genes were selected using the cutoff of FDR<0.1 and $|\log_2\text{FC}|>1.5$. Genes that were
1172 upregulated or downregulated were labelled in red and blue respectively with
1173 corresponding counts.

1174 D. Dot plots showing the top 5 altered cellular and molecular functional categories
1175 derived from DE genes analysis using Ingenuity Pathway Analysis software. Specific
1176 sub-functions within overarching categories are presented as individual dots.

1177 Consistently altered pathways across all four cohorts are indicated in red.

1178 E. Stacked bar plot showing the distribution of 14 hotspot *ESR1* mutations identified in
1179 six independent cohorts using unbiased DNA sequencing approaches. Specific sample
1180 numbers were indicated in the plots. Variants with percentages above 1% were labelled
1181 on the top of each bar.

1182 F. Scatterplot representing enrichment level distribution of 50 hallmark gene sets in 10
1183 Y537S and 8 D538G metastatic tumors (after being normalized against 98 WT
1184 counterparts) from the DFCI cohort. Top enriched pathways from each quartile are
1185 labelled.

1186

1187 **Figure 2. *ESR1* mutant cells exhibit stronger cell-cell adhesion.**

1188 A. Representative images of day 6 hormone deprived MCF7 and T47D spheroids
1189 seeded in 6-well ultra-low attachment (ULA) plates. Images were taken under 1.25x
1190 magnification. Representative experiment from three independent repeats is shown.
1191 B. Bar plot representing day 7 cell numbers of MCF7 or T47D WT and *ESR1* mutant
1192 cells seeded into flat bottom ULA plates. Cell abundance were quantified using Celltiter
1193 Glo. Fluorescence readouts were corrected to background measurements. Each bar
1194 represents mean \pm SD with 10 (MCF7) or 6 (T47D) biological replicates. Representative
1195 experiment from six independent repeats is shown. Dunnett's test was used between
1196 WT and each mutant. (** p<0.01)
1197 C. Left panel: A calcein labelled cell-cell adhesion assay was performed in MCF7 WT
1198 and mutant cells. Adhesion ratios were calculated by dividing the remaining cells after
1199 each wash to the initial readout from unwashed wells. A pairwise two-way ANOVA
1200 between WT and each mutant was utilized. Each point represents mean \pm SD with five
1201 biological replicates. Representative experiment from 17 independent repeats is shown.
1202 Right panel: Adhesion ratios after three washes were extracted from 17 independent
1203 experiments displayed as mean \pm SEM. Dunnett's test was used to compare between
1204 WT and each mutant. (* p<0.05, ** p<0.01)
1205 D. Line plot representing the aggregation ratio of MCF7 cells seeded into round bottom
1206 ULA plates. Cell aggregation processes were followed by the IncuCyte living imaging
1207 system every hour. Spheroid areas were normalized to time 0. Each dot represents
1208 mean \pm SD with eight biological replicates. Representative images after 3 hours of
1209 aggregation are shown across the top panel. Images were captured under 10x
1210 magnification. Representative experiment from five independent repeats is shown. A
1211 pairwise two-way ANOVA between WT and each mutant was utilized. (** p<0.01)
1212 E. Representative images of MCF7 cell cluster status after two hours of flow under
1213 physiological shear stress produced by the ibidi microfluidic system. Images were taken
1214 under 10x magnification. A regional 2x zoom in is presented on the top of each image.
1215 Representative experiment from three independent repeats is shown.
1216 F. Bar graph representing the percentage of MCF7 cells in a cluster based on the
1217 quantification of cluster and single cell numbers from 12 representative images per
1218 group. Each bar represents mean \pm SD. Cell cluster ratios after 2 hours of flow were

1219 further normalized to time 0 to correct for baseline pre-existing clusters. Representative
1220 experiment from three independent repeats is shown. Dunnett's test was used between
1221 WT and mutant cells. (** p<0.01)

1222 G. Bar plots showing the cluster size distribution of MCF7 cells after normalization to
1223 time 0. Each bar represents mean \pm SD from 12 representative images per group.
1224 Representative experiment from three independent repeats is shown. Dunnett's test
1225 was used between WT and each mutant cell type within the same cluster size category.
1226 (** p<0.01).

1227 H. Schematic overview of short-term *in vivo* circulating tumor cell evaluation
1228 experimental procedure.

1229 I. Left panel: Representative images of two-cell clusters (WT) and a multicellular cluster
1230 (Y537S). Images were taken under 40x magnification. Right panel: Stacked bar chart
1231 representing the distribution of cancer cells in each cluster type. This experiment was
1232 performed once. Fisher's exact test was applied to test whether multicellular clusters
1233 were enriched in *ESR1* mutant cells. (** p<0.01)

1234 J. Left panel: Representative images of a WT and Y537S two cell cluster. Lines
1235 connecting the two nuclei centers were indicated. Images were taken under 40x
1236 magnification. Right panel: Dot plot represents the inter-nuclei distance of all two-cell
1237 clusters in MCF7 WT and mutant cells. Measured distances were normalized to the
1238 average radius of both cells of this cluster size to avoid cell size bias. This experiment
1239 was performed once. Mann-Whitney U test was performed between WT and each
1240 mutant cell. (** p<0.01)

1241 K. Schematic overview of *in vivo* metastatic evaluation of *ESR1* mutant cells introduced
1242 via tail vein injections.

1243 L. Representative H&E staining images the tumorous portion of MCF7-Y537S induced
1244 macro-metastatic (macro-met) tumors from 3 different mice. This experiment was
1245 performed once. Images were taken under 20x magnification.

1246 M. Left panel: Dot plots showing the number of macro-met per mouse from MCF7 *ESR1*
1247 WT and mutant cells-injected mice. Pairwise Mann-Whitney U test was used to
1248 compare the macro-met numbers in each mutant group to WT cell-injected groups.
1249 Right panel: Quantification of lung micro-met areas based on human specific CK19

1250 staining quantification. This experiment was performed once. Pairwise Mann-Whitney U
1251 test was applied for statistical analysis. (WT, n=7; Y537S, n=6; D538G, n=7) (* p<0.05)
1252 N. Representative images of micro-metastatic loci on the lung sections of T47D-*ESR1*
1253 mutant cell-injected mice. Images were taken under 10x magnification. Metastatic loci
1254 were indicated with white arrow. This experiment was p once. (WT, n=7; Y537S, n=6;
1255 D538G, n=7) (Blue: nuclei; Red: CK8+18; Green: Human specific CK19)
1256 O. Left panel: Dot plots showing the macro-metastatic counts per mouse from T47D
1257 *ESR1* mutant-injected mice. Pairwise Mann-Whitney U test was used to compare the
1258 macro-met numbers in each mutant group to WT cell-injected groups. Right panel:
1259 Quantification of lung micro-met areas based on CK19 staining and was performed in a
1260 blind manner. This experiment was performed once. Pairwise Mann-Whitney U test was
1261 applied for statistical analysis. (N=1, * p<0.05)
1262 P. Representative images of CTCs clusters detected through the CellSearch Platform
1263 after EpCAM dependent enrichment (Pink: nuclei, Green: CK8/CK18/CK 19). Image
1264 resolution and magnification were achieved in accordance with the CellSearch Platform.
1265 Q. Mosaic plot showing the association between *ESR1* genotype status and clustered
1266 CTCs. A significant positive association was observed by Fisher's exact test between
1267 *ESR1* mutations and high CTC cluster burden. (CTC cluster > 4).
1268 R. Kaplan Meier plot representing the impact of clustered CTCs in terms of Overall
1269 Survival (OS). Patients with clustered CTCs > 4 experienced the worse prognosis in
1270 terms of OS both with respect to those without clusters and those with clusters but with
1271 ≤ 4 clustered CTCs ($P < 0.0001$). Patients at risk are reported at each time point. Log
1272 rank test was to compare the survival curves of the two patient subsets.
1273

1274 **Figure 3. Desmosome and gap junction adhesome reprogramming confers**
1275 **enhanced adhesive properties in *ESR1* mutant cells.**

1276 A. Gene Set Variation Analysis (GSVA) scores of desmosome and gap junction gene
1277 sets enrichment in MCF7 and T47D *ESR1* mutant vs WT cell RNA-seq data sets. Each
1278 cell type has four biological replicates. Dunnett's test was used to test the significance
1279 between WT and mutant cell lines. (** p<0.01)

1280 B. Heatmaps showing all desmosome and gap junction component genes in MCF7 and
1281 T47D *ESR1* mutant cells. Data were extracted from RNA-sequencing results with four
1282 biological replicates. Color scale represents the Log2 fold changes in each mutant
1283 normalized to WT counterparts using the $\log_2(\text{TPM}+1)$ expression matrix. Genes with
1284 counts=0 in more than one replicate in each cell type were filtered out of analysis.
1285 Genes with a $\log_2\text{FC}>1.2$ and a $p<0.05$ in at least one group are labelled in red.
1286 C. Western blot validation of the expression level of *DSG2*, *DSC1*, *PKP1*, Cx43 and
1287 Cx26 in MCF7 WT and *ESR1* mutant cells after hormone deprivation. Tubulin was
1288 blotted as a loading control. Representative blots from three independent repeats was
1289 shown for each protein.
1290 D. qRT-PCR validation of selected altered candidate desmosome and gap junction
1291 genes in MCF7 *ESR1* mutant cells. $\Delta\Delta\text{Ct}$ method was used to analyze relative mRNA
1292 fold changes normalized to WT cells and *RPLP0* levels were measured as an internal
1293 control. Each bar represents mean \pm SD with biological triplicates. This experiment was
1294 a representative from four independent repeats. Dunnett's test was used to compare the
1295 gene expression between WT and each mutant. (* $p<0.05$, ** $p<0.01$)
1296 E. Representative images of immunofluorescence staining showing the distribution of
1297 desmoglein 2 (*DSG2*) in MCF7 WT and *ESR1* mutant cells. Images were taken under
1298 20x magnification. A 2x zoom in of each image is presented. Right lower panel: *DSG2*
1299 signal intensities were quantified and normalized to cell numbers in each image. Data
1300 from 20 regions within the collected images were combined from four independent
1301 experiments. Mean \pm SD is presented in each plot. Dunnett's test was used to test the
1302 significance between WT and mutant cells. (** $p<0.01$)
1303 F. Box plots representing GSVA scores of the enrichment of the top desmosome and
1304 gap junction candidate genes (genes with $\log_2\text{FC}>2$ in at least one mutant line) in
1305 patient matched primary-metastatic paired samples. Delta GSVA score of each sample
1306 was calculated by subtracting the scores of primary tumors from the matched metastatic
1307 tumors. Four quantiles are shown in each plot. Mann-Whitney U test was performed to
1308 compare the Delta GSVA scores between *ESR1* WT (n=44) and mutation (n=7)
1309 harboring tumors. (* $p<0.05$)

1310 G & J. Representative images of cell cluster status after two hours of flow under
1311 physiological shear stress in the ibidi microfluidic system, with or without 300 μ M of the
1312 desmosomal blocking peptide (G) or 100 μ M of carbenoxolone (J) treatment. Images
1313 were taken under 10x magnification. This experiment was a representative from two
1314 (desmosome peptide treatment) and three (CBX treatment) independent repeats.
1315 H & K. Bar graphs representing the T0 normalized percentage of cells in cluster status
1316 after quantification of cluster and single cell numbers under each treatment. Each bar
1317 represents mean \pm SD quantified from 12 images per group. This experiment was a
1318 representative from two (desmosome peptide treatment) and three (CBX treatment)
1319 independent repeats. Student's t test was used to examine the effects of treatment
1320 between each group's cluster ratio. (** p<0.01)
1321 I & L. Bar graphs representing the T0 normalized 2 cell and greater than 5 cell cluster
1322 percentages under each treatment. Each bar represents mean \pm SD quantified from 12
1323 images per group. This experiment was a representative from two (desmosome peptide
1324 treatment) and three (CBX treatment) independent repeats. Pairwise student's t test
1325 was used to examine the effects of treatment between each group's cluster ratio. (**
1326 p<0.01)
1327 M. Bar graphs representing qRT-PCR measurement of *DSC1*, *DSC2*, *GJA1*, *GJB2* and
1328 *GJB5* mRNA levels in MCF7 WT and *ESR1* mutant cells following siRNA knockdown of
1329 *ESR1* for 7 days. $\Delta\Delta Ct$ method was used to analyze relative mRNA fold changes
1330 normalized to WT cells and *RPLP0* levels were measured as an internal control. Each
1331 bar represents mean \pm SD with three biological replicates. Representative experiment
1332 from three independent repeats is displayed. Student's t test was used to compare the
1333 gene expression between scramble and knockdown groups of each cell type. (* p<0.05,
1334 ** p<0.01)
1335 N & O. Western blot validation of the expression level of ER, Cx43 and cFOS in MCF7
1336 WT and *ESR1* mutant cells after seven days of *ESR1* knockdown (N) or three days of
1337 20 μ M T-5224 treatment (O). Tubulin was blotted as a loading control. Representative
1338 blot from three (N) and five (O) independent repeats is displayed.
1339 P. Screen shot of H3K27ac and H3K4me2 binding peaks at proximity to genomic *DSC1*
1340 and *DSG1* loci in MCF7 parental cells. ChIP-seq data were visualized at WashU

1341 Genome Browser based on public available data set from ENCODE (H3K4me2:
1342 ENCSR875KOJ ; H3K27ac: ENCSR752UOD). Y axis represents the binding intensity of
1343 each ChIP-seq data set. Selected peaks for ChIP-qPCR assessment in Q were
1344 indicated.

1345 Q. Bar graph showing the fold enrichment levels of the two active histone modification
1346 markers at the two selected peaks around *DSC1* and *DSG1* gene loci illustrated in P.
1347 Each bar represents mean \pm SD from biological triplicates. Fold enrichment levels were
1348 calculated by normalizing to IgG controls and further normalized to WT levels. This
1349 experiment is representative from two independent repeats. Dunnett's test was used
1350 within each group. (N=2, * p<0.05, ** p<0.01)

1351

1352 **Figure 4. *ESR1* mutant cells show diminished ECM adhesion and enhanced
1353 invasion via an altered *TIMP3-MMP* axis.**

1354 A. Gene set enrichment plots showing the comparison of enrichment levels of the
1355 "KEGG ECM Receptor Interaction" gene set (MSigDB, M7098) between WT and mutant
1356 tumors in DFCI cohort. (98 *ESR1* WT and 32 mutant tumors)

1357 B. Heatmap representation of adhesion ratio on 7 ECM components performed with
1358 MCF7 and T47D *ESR1* WT and mutant cells. Adhesion ratio of each condition with
1359 biological quadruplicates was quantified by dividing the number of remaining cells after
1360 washing to the original total cells plated. All data was further normalized to WT cells
1361 within each cell line. This experiment was performed once. Dunnett's test was applied to
1362 each condition of each cell line. (* p<0.05, **p<0.01)

1363 C. Representative images *ESR1* WT and mutant cells remaining on collagen I after
1364 three PBS washes. Images were taken using 4x magnification. Experiment displayed is
1365 representative from three independent repeats.

1366 D. Quantification of adhesion ratios on collagen I in each cell type. Bar graphs represent
1367 the mean \pm SD with four biological replicates in each group. Dunnett's test was utilized
1368 within each cell line to compare WT and mutant adhesion ratios. Experiment displayed
1369 is representative from 12 (MCF7) and 11 (T47D) independent repeats. (* p<0.05, **
1370 p<0.01)

1371 E. Volcano plots showing the alterations of 84 ECM adhesion genes in all mutant cell
1372 types in a pairwise comparison to the WT counterparts. Genes were pre-filtered with an
1373 average Ct<35 in at least one group. An FDR<0.1 was considered as a significantly
1374 altered gene in *ESR1* mutant cells. Overlapping downregulated (blue) or upregulated
1375 (red) genes between the two mutants of each cell line were further highlighted, with
1376 gene name labels for the top targets. Top changed genes in each T47D mutant cells
1377 were labelled in green. This experiment was performed once.

1378 F. Venn diagrams showing the consistently differentially expressed genes between the
1379 two mutant variants within each cell line. *TIMP3* was highlighted as the only overlapping
1380 gene in all four *ESR1* mutant cell types.

1381 G. qRT-PCR validation of *TIMP3* expression in WT and *ESR1* mutant cells. Ct values
1382 were normalized to *RPLP0* and further normalized to WT cells. Bar graphs represent
1383 the mean \pm SD with biological triplicates in each group. Representative experiment from
1384 seven independent repeats is shown. Dunnett's test was utilized within each cell line. (*
1385 p<0.05, ** p<0.01)

1386 H. Western blot validation of *TIMP3* from whole cell lysates after hormone deprivation.
1387 Tubulin was used as a loading control. Representative experiment from six independent
1388 repeats is shown.

1389 I & J. Quantification of adhesion ratios on collagen I in each mutant variant following
1390 transfection of pcDNA empty vector or *TIMP3* plasmids in MCF7 (I) and T47D (J) cell
1391 models. Bar graphs represent the mean \pm SD from 5 (MCF7) and 7 (T47D) biological
1392 replicates. Representative experiment from four independent repeats is shown.
1393 Student's t test was used to compare the empty vector and *TIMP3* overexpressing
1394 groups. (* p<0.05, ** p<0.01)

1395 K & L. Graphical view of pan-MMP FRET kinetic assay. MMPs in MCF7 (K) and T47D
1396 (L) cell lysates were pre-activated and mixed with MMP substrates. Fluorescence was
1397 measured in a time course manner and normalized to T0 baseline and further
1398 normalized to WT cell readouts. Each point represents the mean \pm SD value from three
1399 biological replicates. Representative experiment from four independent repeats is
1400 shown. Pairwise two-way ANOVA between WT and each mutant cell type was
1401 performed. (* p<0.05, ** p<0.01)

1402 M. Top panel: Representative images of the spheroid-based collagen invasion assay in
1403 *ESR1* WT and mutant cell models. MCF7 and T47D spheroids were mixed in collagen I
1404 for 4 and 6 days, respectively. Bright field images were taken accordingly with 10x
1405 magnification. Bottom panel: Quantification of invasive areas within images. Invasive
1406 areas were calculated by subtracting each original spheroid area from the
1407 corresponding endpoint total area. Each bar represents mean \pm SD with 10 biological
1408 replicates. Experiments displayed are representative from three independent repeats
1409 from each cell line. Dunnett's test was used to compare the difference between WT and
1410 mutant cells. (* p<0.05, ** p<0.01)

1411 N & P. Representative images of the spheroid-based collagen invasion assay with
1412 different doses of Marimastat treatment in MCF7 (N) and T47D (P) cell models for 4 and
1413 6 days, respectively. Images were taken under 10x magnification. Experiments
1414 displayed are representative from three independent repeats from each cell line.
1415 Q & O. Quantification of corresponding invasive areas from 4N and 4P. Experiments
1416 displayed are representative from three independent repeats from each cell line.
1417 Student's t test was used to compare the effects of Marimastat treatment to vehicle
1418 control. (* p<0.05, ** p<0.01)

1419

1420 **Figure 5. *De novo* FOXA1-mediated Wnt pathway activation enhances migratory
1421 property of the T47D-D538G cells.**

1422 A & B. Representative images (A) and quantification (B) of wound scratch assay of
1423 T47D WT and *ESR1* mutant cells performed using IncuCyte living imaging system over
1424 72 hours. The migratory region normalized to T0 are labelled in blue. Images were
1425 taken under 10x magnification. Cell migration rates were quantified based on relative
1426 wound densities with 8 biological replicates. Representative experiment from 11
1427 independent repeats is shown. Pairwise two-way ANOVA between WT and each mutant
1428 was performed. (** p<0.01)

1429 C. Representative magnified images of the migratory edge of each group in wound
1430 scratch assays in A.

1431 D & E. Representative images (D) and quantification (E) of spheroid collective migration
1432 assays in T47D mutant cells. T47D cells were initially seeded into round bottom ULA

1433 plates to form spheroids, which were then transferred onto collagen I coated plates.
1434 Collective migration was measured after 4 days. The migratory edge of each spheroid is
1435 circled with a white line. Migratory distances were calculated based on the mean radius
1436 of each spheroid normalized to corresponding original areas. Representative
1437 experiment from three independent repeats is shown. Dunnett's test was used for
1438 statistical analysis. (** p<0.01)

1439 F. Dot plots representing the enrichment distribution of the 50 MSigDB curated Hallmark
1440 gene sets in T47D-Y537S and T47D-D538G models normalized to WT cells.
1441 Significantly enriched gene sets (FDR<0.25) are highlighted in red, with names labeled
1442 in the venn diagram plot on the right panel. Gene sets enriched in Y537S and D538G
1443 cell models are in green and blue circles respectively.

1444 G. Immunoblot detection of β -catenin, phospho-GSK3 β (Ser9), phospho-GSK3 α (Ser21)
1445 total GSK3 β and total GSK3 α levels in T47D WT and mutant cells after hormone
1446 deprivation. Tubulin was blotted as a loading control. Representative blots from three
1447 independent repeats is displayed for each protein.

1448 H. Quantification of IncuCyte wound scratch assay with or without 5 μ M LGK974
1449 treatment for 72 hours. The migratory region normalized to T0 are labelled in blue.
1450 Images were taken under 10x magnification. Cell migration rates were quantified based
1451 on relative wound densities with eight biological replicates. Representative experiment
1452 from three independent repeats is shown. Pairwise two-way ANOVA between WT and
1453 each mutant was performed. (** p<0.01)

1454 I. IncuCyte migration assay with combination treatment of four different doses of
1455 LGK974 and Fulvestrant in T47D-D538G cells. Inhibition rates were calculated using
1456 the wound density at 48 hours normalized to vehicle control with values labelled using
1457 color scales in the heatmap. Positive Bliss scores are considered a synergistic
1458 combination. Representative experiment from three independent repeats is shown.

1459 J. Dot plot representing the fold changes of all Wnt signaling component genes in both
1460 T47D *ESR1* mutant cell models normalized to WT cells. The blue dotted frame
1461 highlights the unique T47D-D538G enriched genes as well as genes that are enriched
1462 in both mutants, but with a larger magnitude of enrichment in the T47D-D538G cells.

1463 K & L. Immunoblot validation of Fulvestrant-induced ER degradation (K) and FOXA1
1464 knockdown (L). Cell lysates were subjected to ER and FOXA1 detection. Tubulin was
1465 blotted as a loading control. These validation experiments were performed once.
1466 M & N. Wound scratch assay in T47D-D538G and WT cells with 1 μ M of Fulvestrant
1467 treatment (M) or knockdown of FOXA1 (N) for 72 hours. Cell migration rates were
1468 quantified based on wound closure density. For fulvestrant treatment, data were merged
1469 from 3 (WT) or 6 (D538G) independent experiments. For FOXA1 knockdown,
1470 representative result from three independent repeats is displayed. Pairwise two-way
1471 ANOVA between siScramble/siFOXA1 or vehicle/Fulvestrant conditions in each cell
1472 type was performed. (* p<0.05, ** p<0.01)
1473 O. PCA plot showing the FOXA1 peak distribution of T47D WT, WT+E2, T47D-Y537S
1474 and T47D-D538G groups.
1475 P. Heatmaps representing the comparison of FOXA1 binding intensities in T47D-D538G
1476 mutants to FOXA1 binding in WT cells. Displayed in a horizontal window of \pm 2kb from
1477 the peak center. The pairwise comparison between WT and mutant samples was
1478 performed to calculate the fold change (FC) of intensities. Binding sites were sub-
1479 classified into sites with increased intensity (FC>2), decreased intensity (FC<-2), and
1480 non-changed intensity (-2<FC<2). Percentages of each subgroup are labelled on the
1481 heatmaps.
1482 Q. Bar charts showing the percentage of ATAC peaks overlapping (black) or not
1483 overlapping (grey) with FOXA1 binding sites in T47D-WT, T47D-Y537S and T47D-
1484 D538G cells.
1485 R. Left panel: Venn diagram showing the intersection of genes annotated from dually
1486 gained ATAC and FOXA1 peaks (\pm 3kb of TSS with 200kb of the peak flank) and RNA-
1487 seq differentially expressed non-canonical ligand-independent genes (gene with |fold
1488 change|>2, FDR<0.005 in D538G vs WT excluding genes with |fold change|>1.5,
1489 FDR<0.01 in WT+E2 vs WT groups). Intersected genes are indicated in the right panel.
1490 S. Wound scratch assay in T47D-WT and T47D-D538G cells with or without prior
1491 transfection of a dominant negative *TCF4* plasmid for 72 hours. Pairwise two-way
1492 ANOVA between vehicle and treatment conditions was performed. Data from one

1493 representative experiment of three independent experiments (each with six biological
1494 repeats) is shown. (** p<0.01)

1495

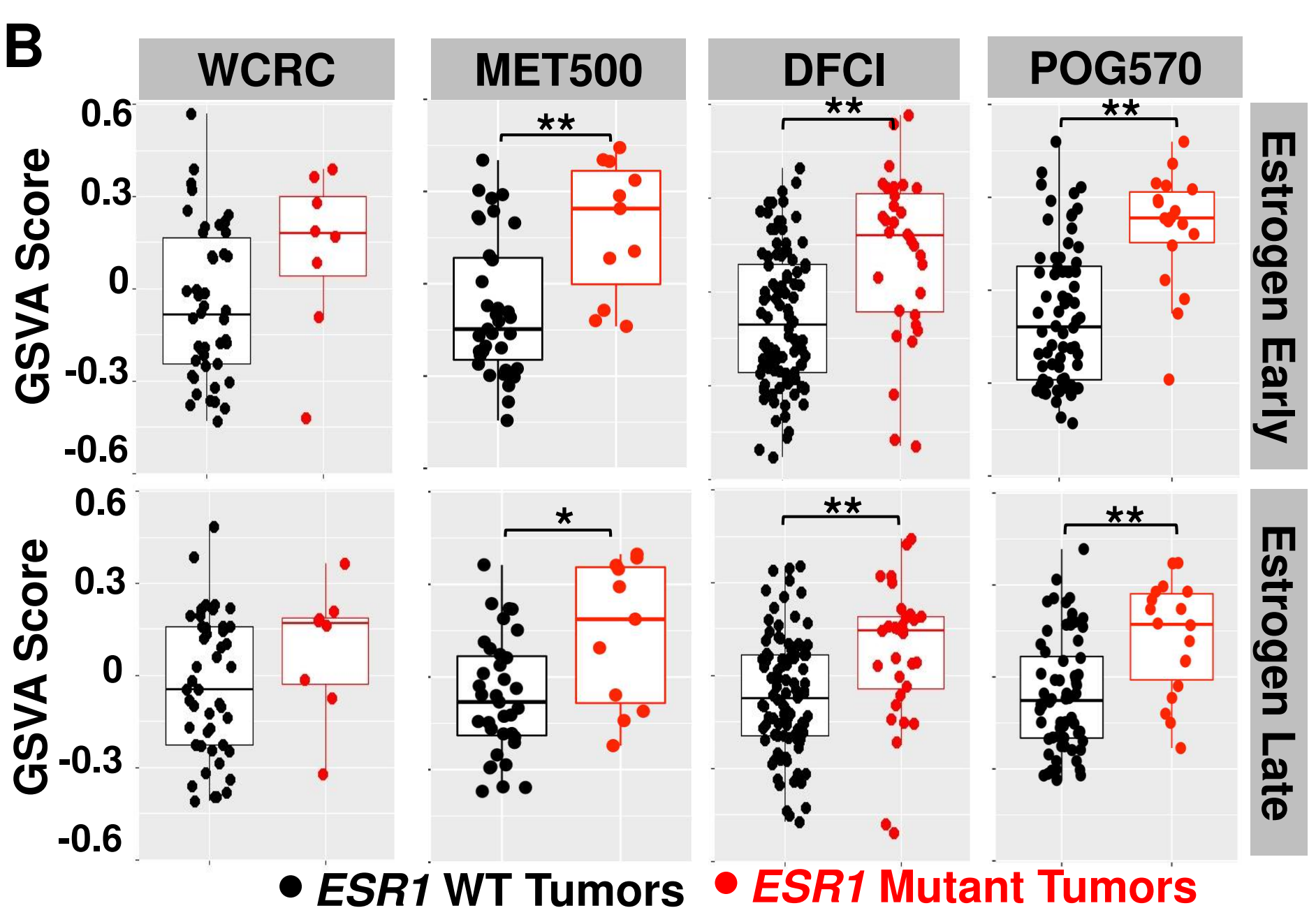
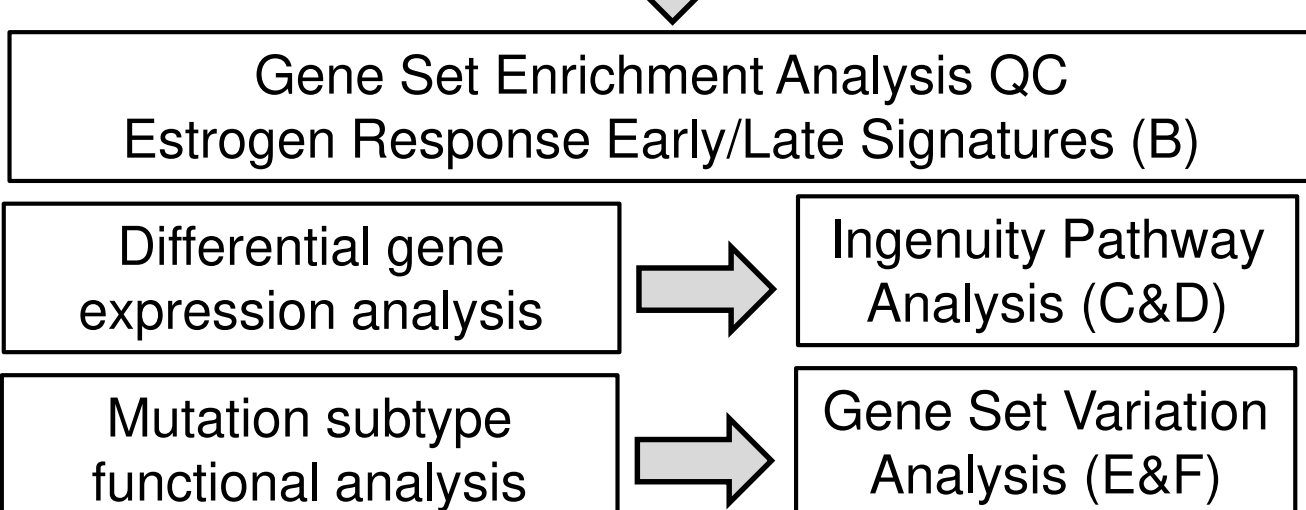
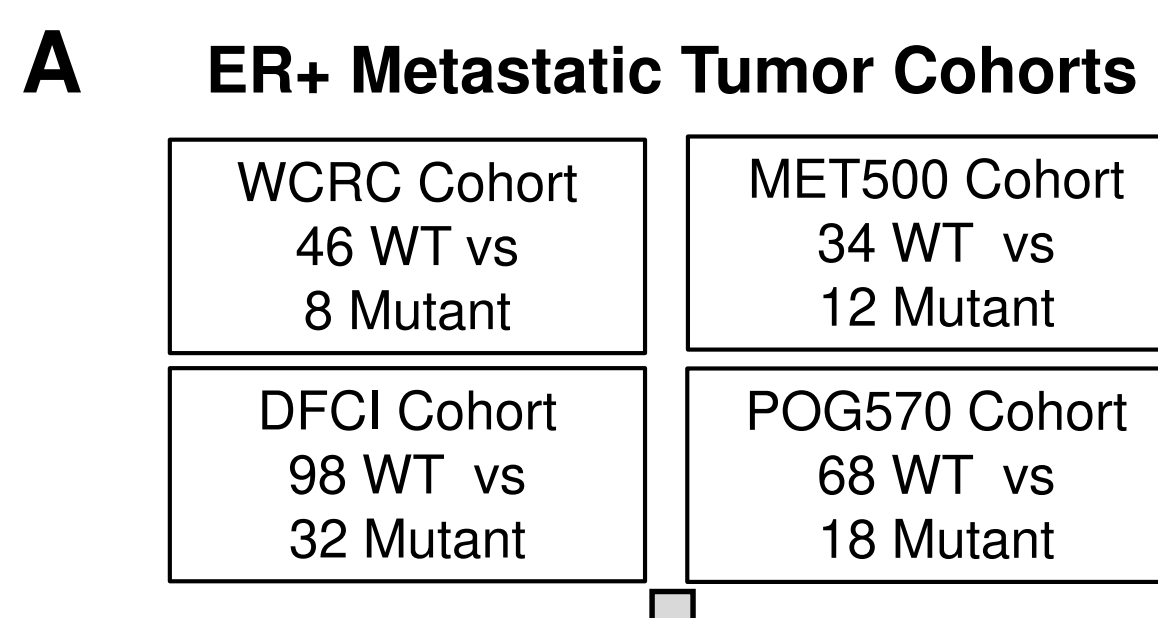
1496 **Figure 6. Schematic model of *ESR1* mutation-driven breast cancer metastases.**

1497 Mutated ER triggers differential gene regulatory reprogramming through 1) ligand-
1498 independent transcriptional gene activation or repression, 2) secondary transcriptional
1499 regulation and 3) FOXA1-driven epigenetic remodeling. Ligand independent
1500 transcription constitutively induces or represses canonical ER regulated sites (e.g.
1501 *TIMP3*). Secondary transactivation induces gene expression indirectly via activation of
1502 an intermediate regulator (e.g. *GJA1*). Novel epigenetic remodeling includes *de novo*
1503 FOXA1 redistribution and increased chromatin accessibility at specific gene loci (e.g.
1504 *TCF4*). Consequently, increased desmosome and gap junction expression, *TIMP3*-
1505 MMP axis alteration and hyperactivation of the Wnt pathway results in enhanced cell-
1506 cell adhesion, collagen invasion, migration and decreased cell-ECM adhesion,
1507 ultimately facilitating metastases of *ESR1* mutant cells. Corresponding therapeutic
1508 vulnerabilities can be efficiently targeted by carbenoxolone, marimatsat and LGK974.
1509 These mechanisms are highly context dependent with phenotypes labeled for specific
1510 cell line models.

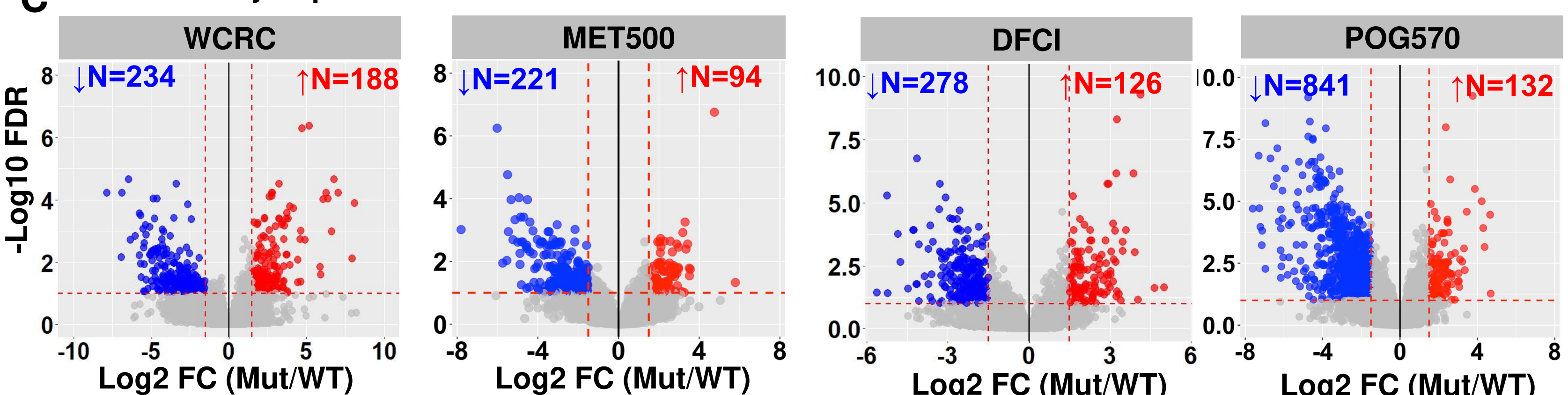
1511

1512

1513



C Differentially Expressed Genes



D Top 5 Altered Molecular & Cellular Functions

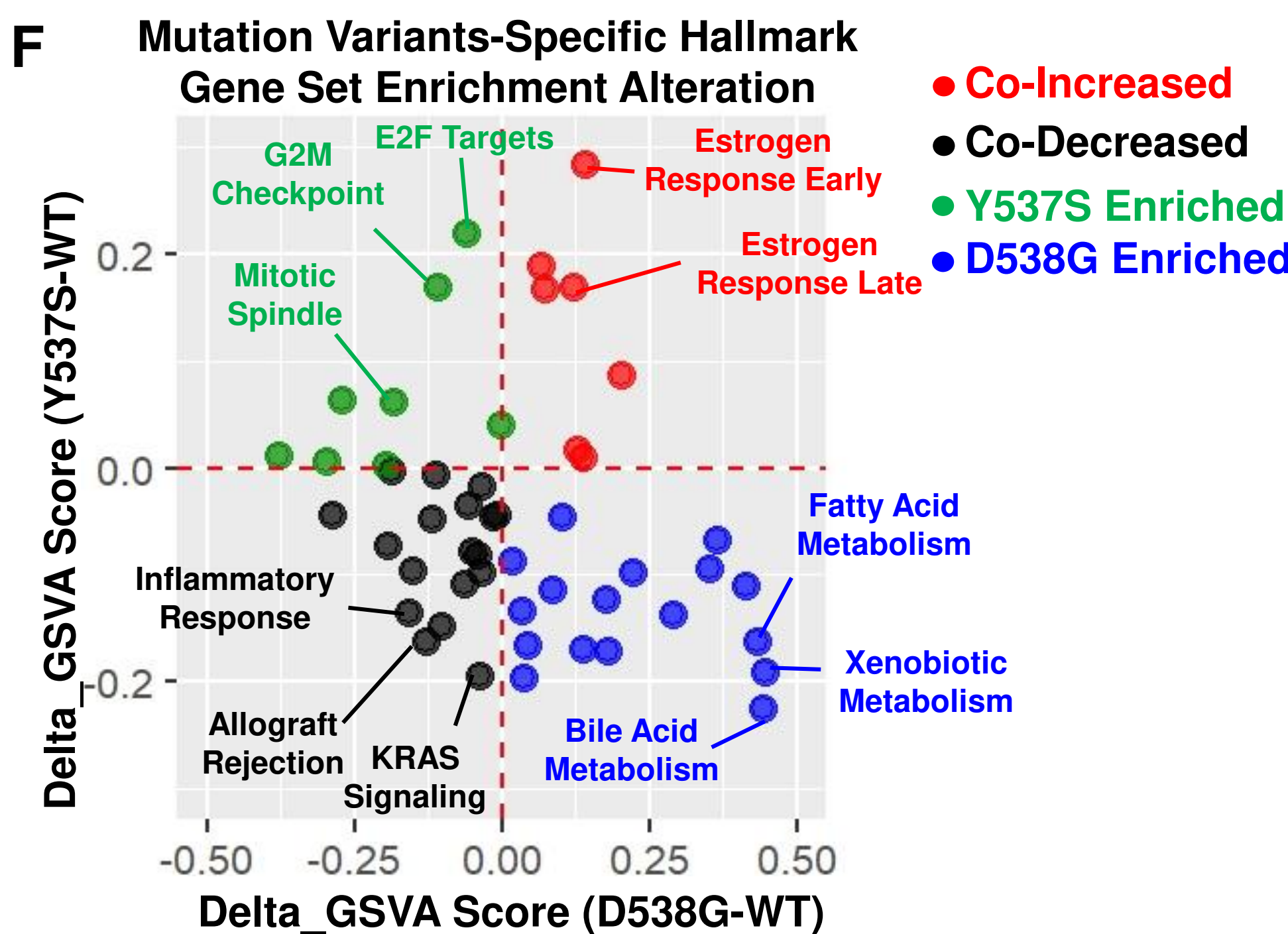
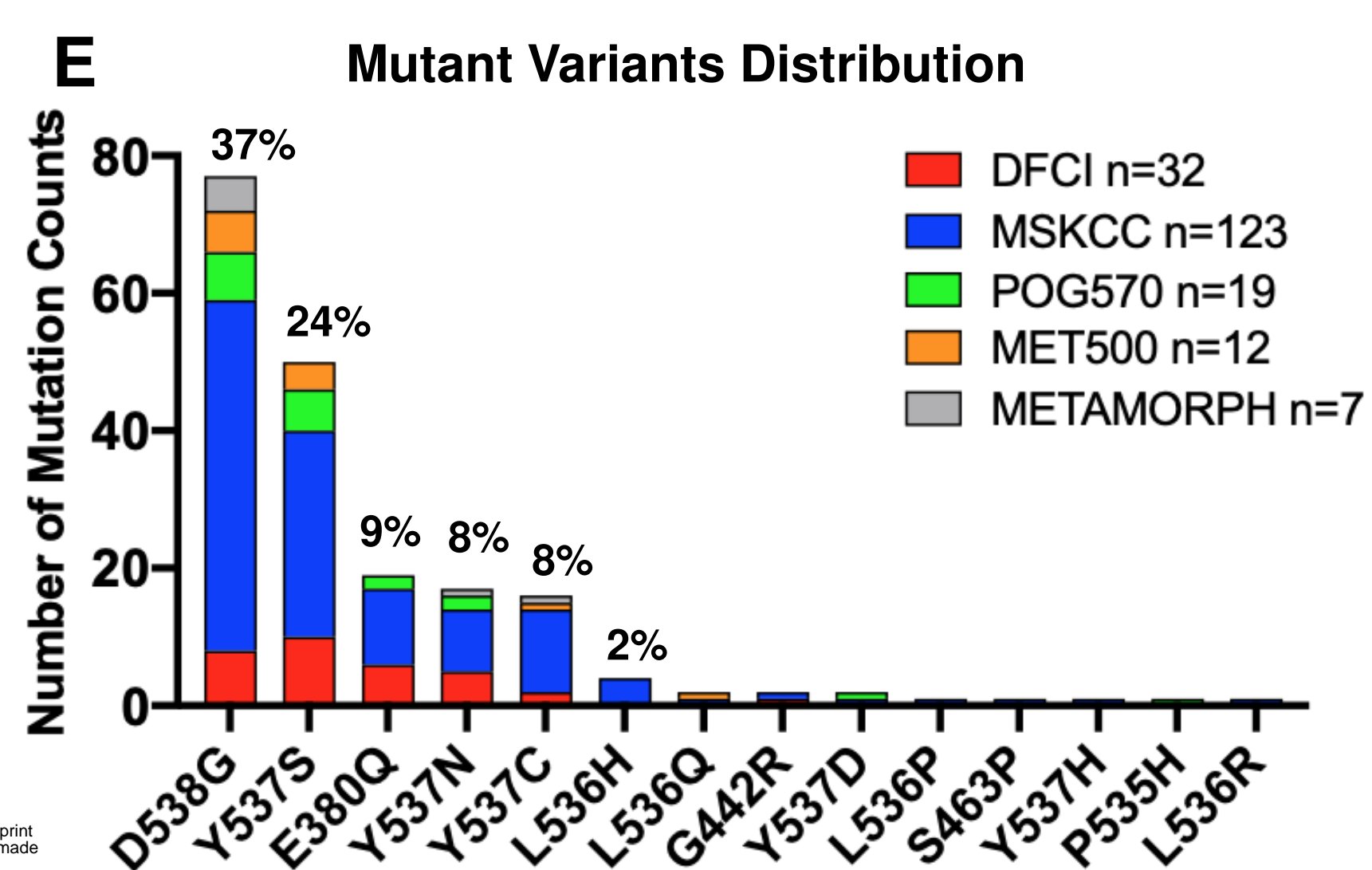
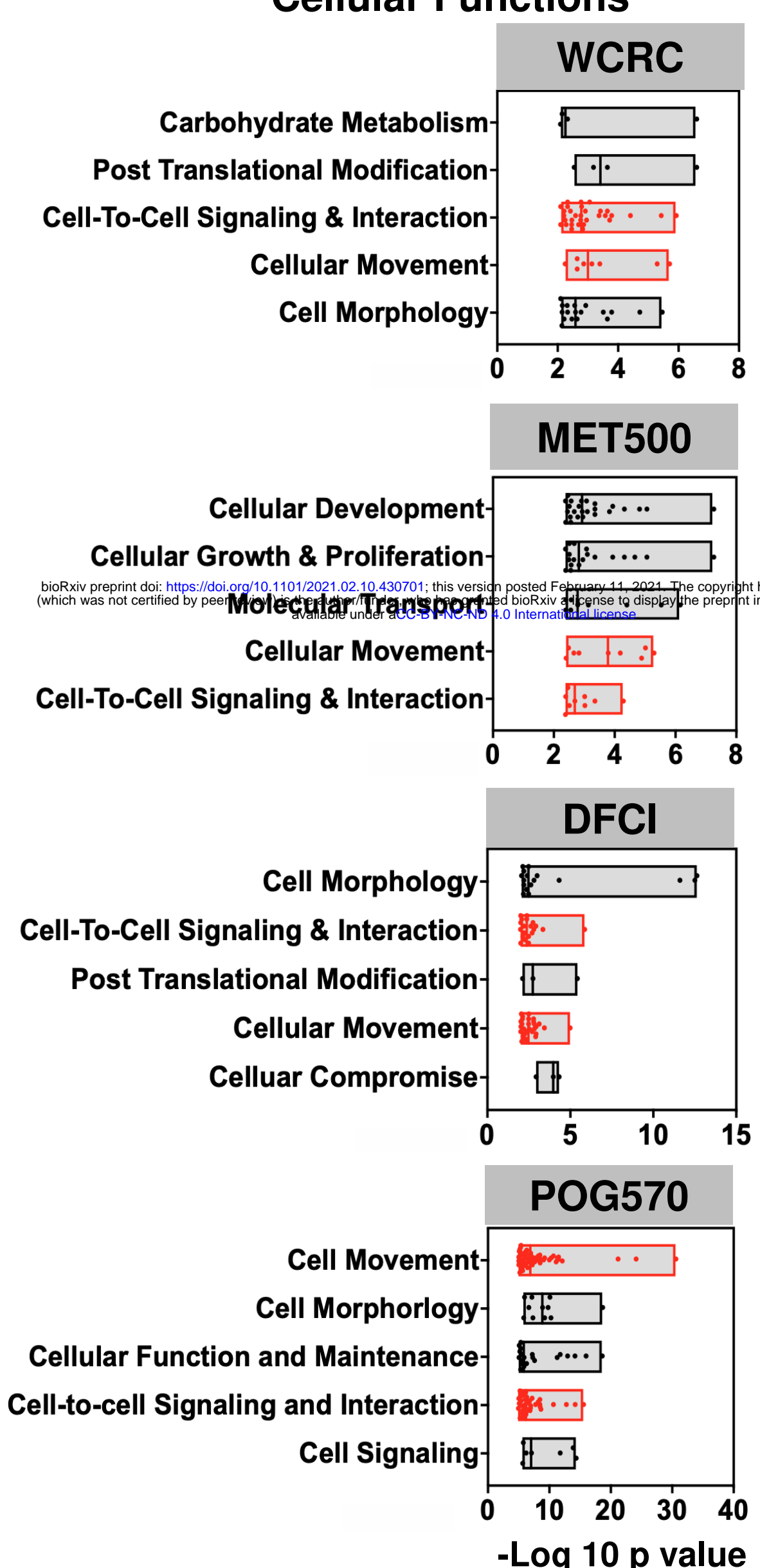


Figure 1. Transcriptomic landscape of *ESR1* mutant metastatic breast cancers.

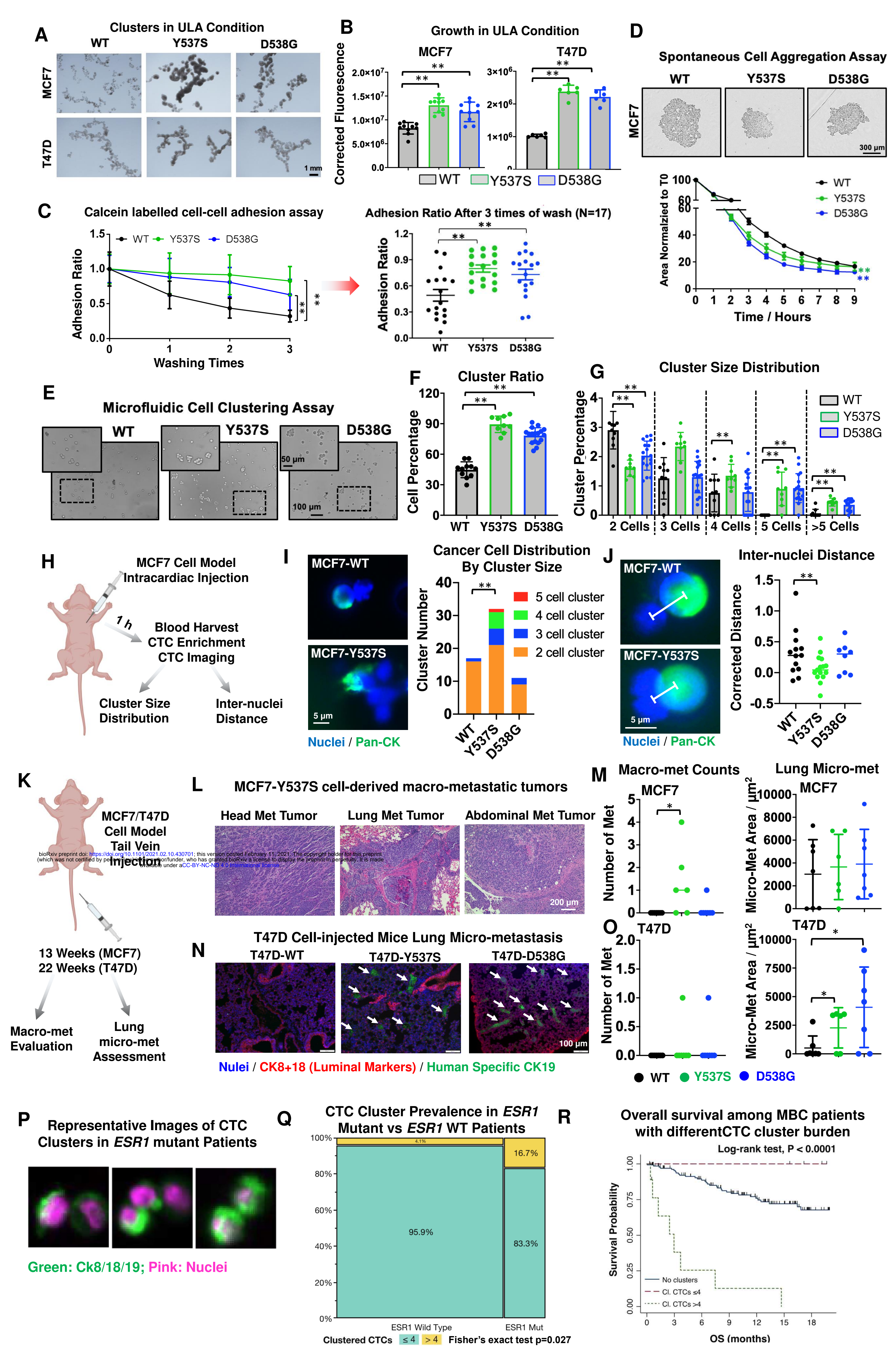


Figure 2. *ESR1* mutant cells exhibit stronger cell-cell adhesion

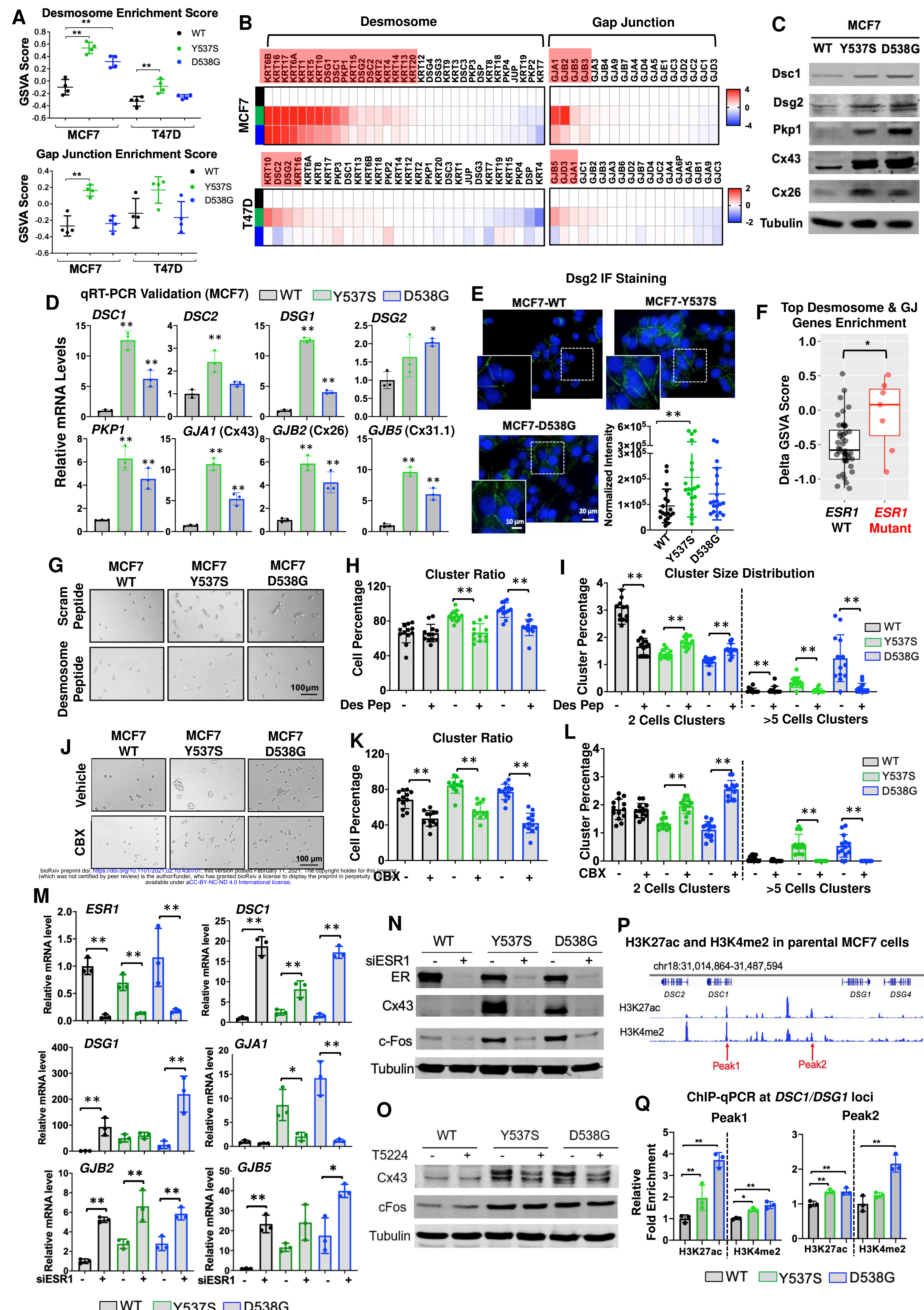


Figure 3. Desmosome and gap junction adhesome reprogramming confers enhanced adhesive properties in *ESR1* mutant cells.

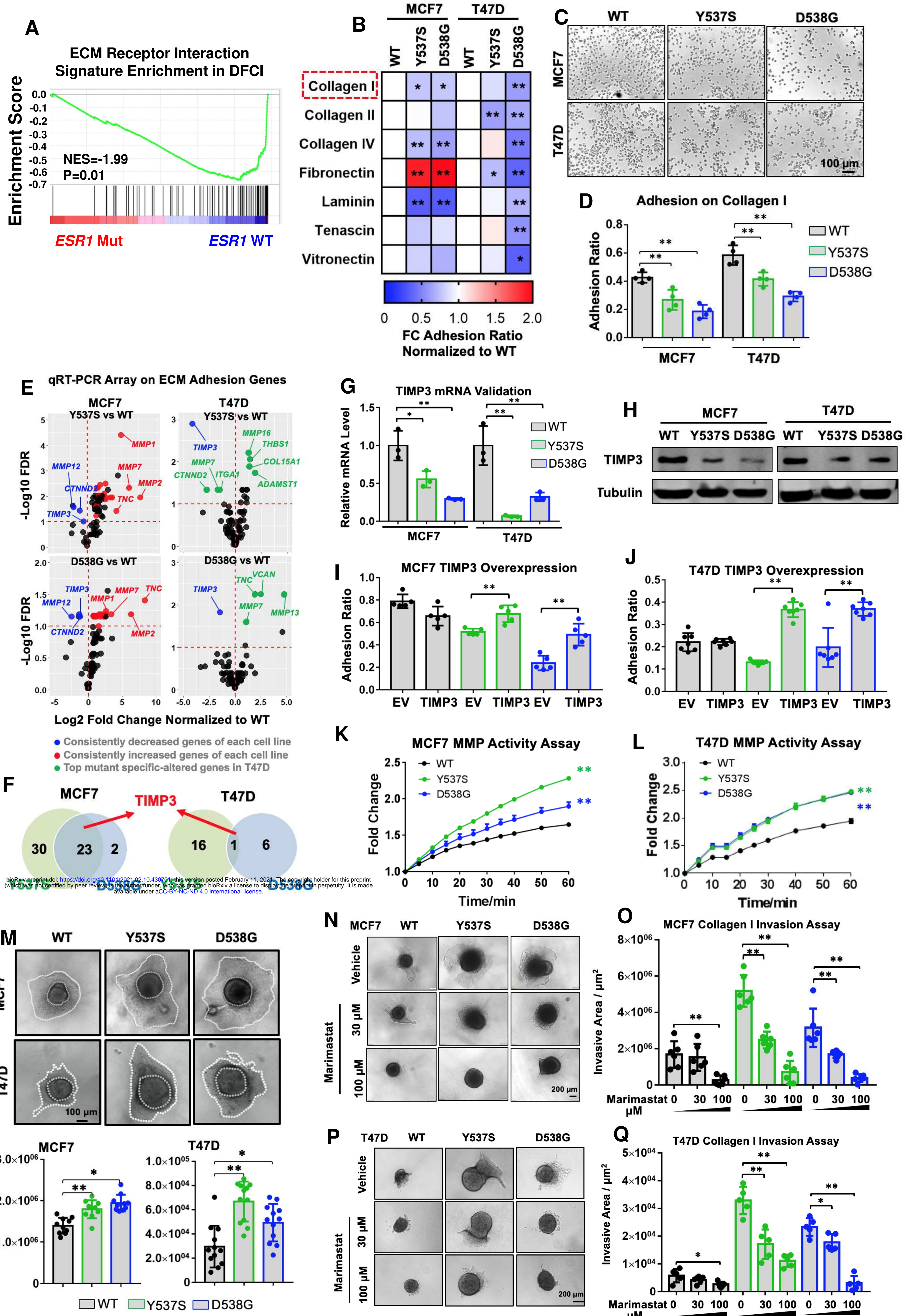


Figure 4. *ESR1* mutant cells show diminished ECM adhesion and enhanced invasion via altered *TIMP3*-MMP axis.

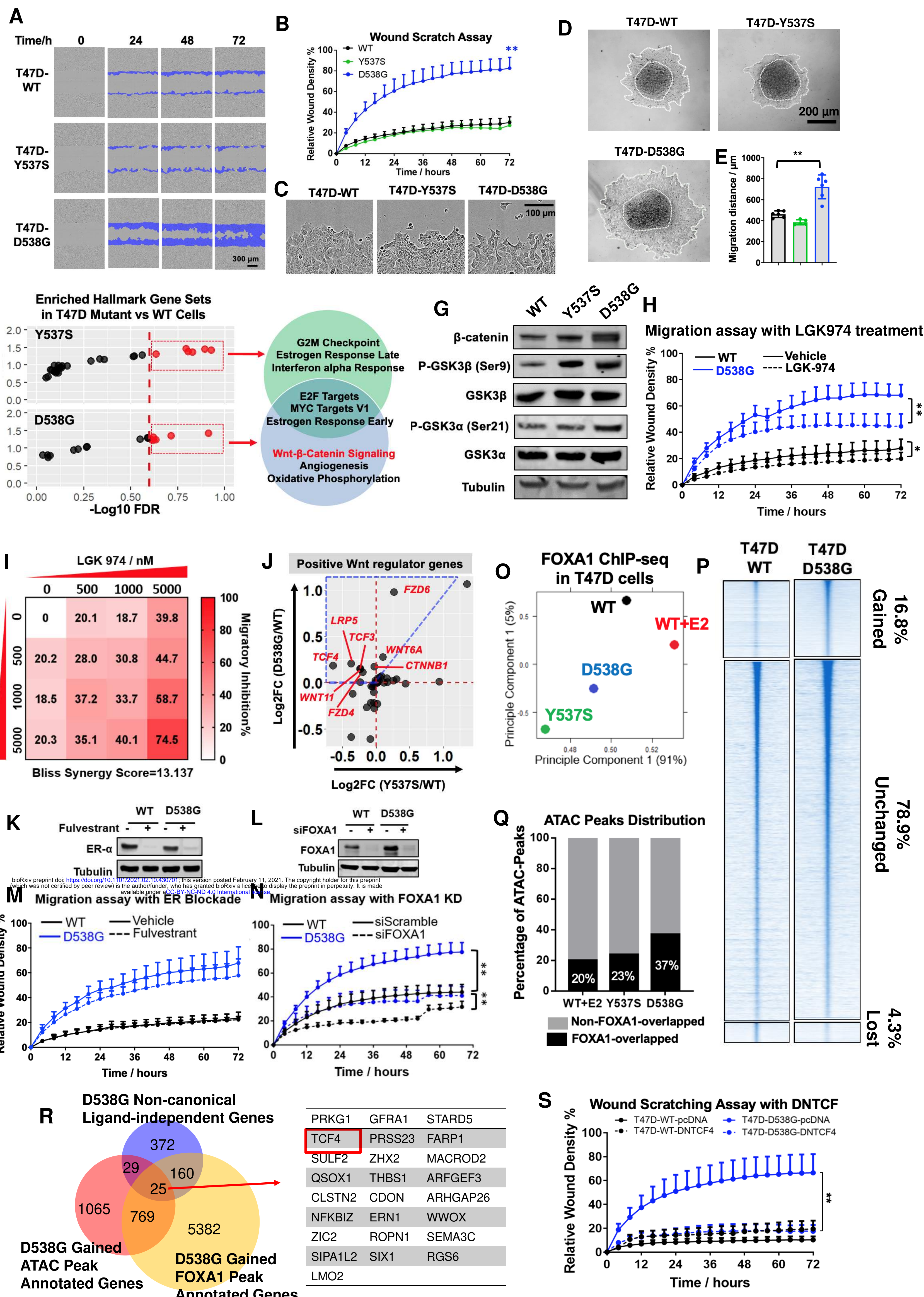


Figure 5. D538G *ESR1* mutant cells escalate migratory properties via Wnt hyperactivation.

PRKG1	GFRA1	STARD5
TCF4	PRSS23	FARP1
SULF2	ZHX2	MACROD2
QSOX1	THBS1	ARFGEF3
CLSTN2	CDON	ARHGAP26
NFKBIZ	ERN1	WWOX
ZIC2	ROPN1	SEMA3C
SIPA1L2	SIX1	RGS6
LMO2		

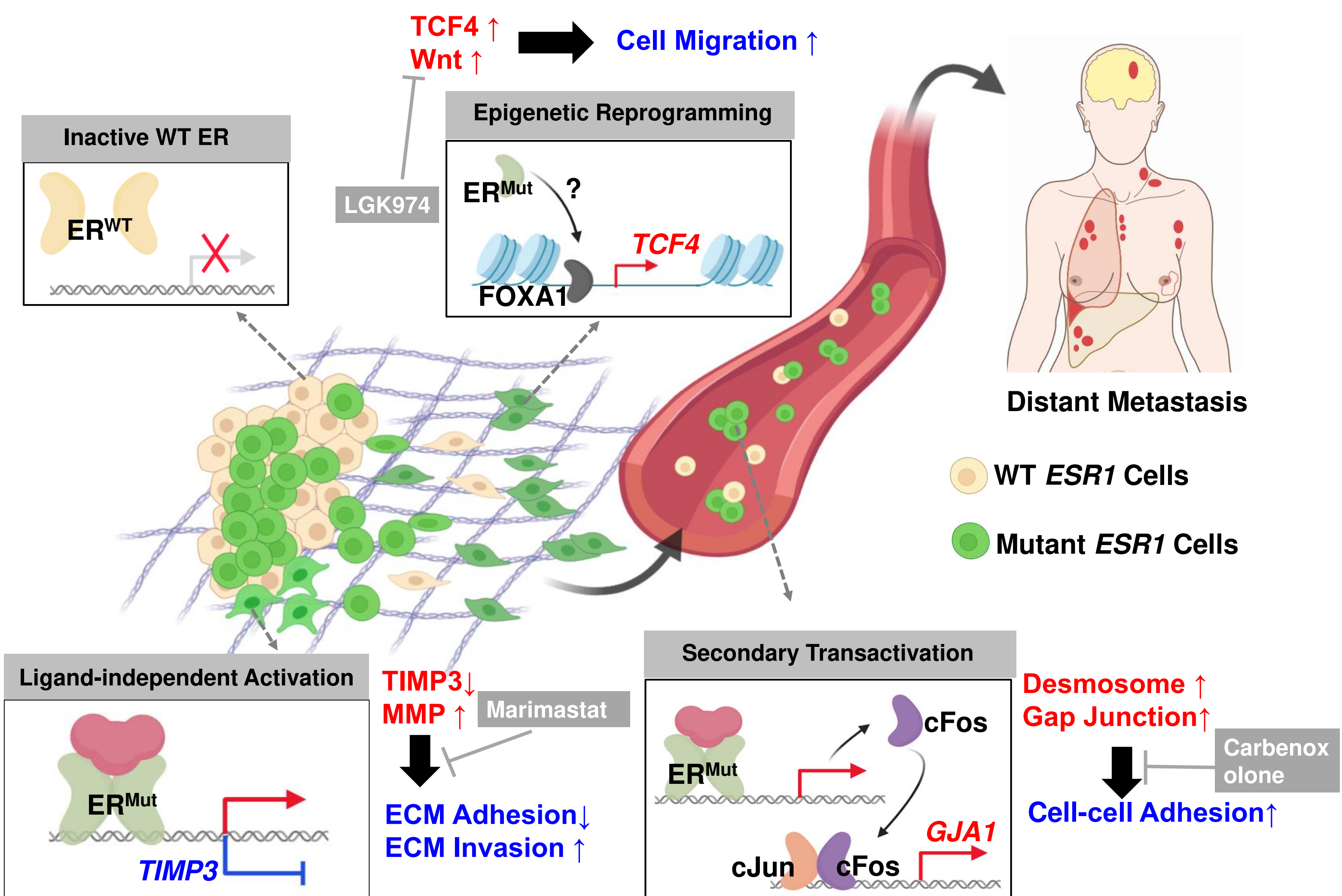


Figure 6. Schematic Model of *ESR1* mutation-driven metastases.

bioRxiv preprint doi: <https://doi.org/10.1101/2021.02.10.430701>; this version posted February 11, 2021. The copyright holder for this preprint (which was not certified by peer review) is the author/funder, who has granted bioRxiv a license to display the preprint in perpetuity. It is made available under aCC-BY-NC-ND 4.0 International license.